

Electronic Supplementary Information (ESI)

Engineering metal-metal oxide surfaces for high-performance oxygen reduction on Ag-Mn electrocatalysts

José A. Zamora Zeledón^{a,b}, G. T. Kasun Kalhara Gunasooriya^c, Gaurav A. Kamat^{a,b}, Melissa E. Kreider^{a,b}, Micha Ben-Naim^{a,b,†}, McKenzie A. Hubert^{a,b}, Jaime E. Avilés Acosta^{b,d}, Jens K. Nørskov^c, Michaela Burke Stevens^{a,b,}, and Thomas F. Jaramillo^{a,b,*}.*

a. Department of Chemical Engineering, Stanford University, 443 Via Ortega, Stanford, California 94305, United States

b. SUNCAT Center for Interface Science and Catalysis, SLAC National Accelerator Laboratory, 2575 Sand Hill Road, Menlo Park, California 94025, United States

c. Catalysis Theory Center, Department of Physics, Technical University of Denmark, 2800 Kongens Lyngby, Denmark

d. Department of Materials Science and Engineering, Stanford University, 496 Lomita Mall, Stanford, California 94305, United States

† Present Address: Materials Science Division, Lawrence Livermore National Laboratory, Livermore, California 94550, United States

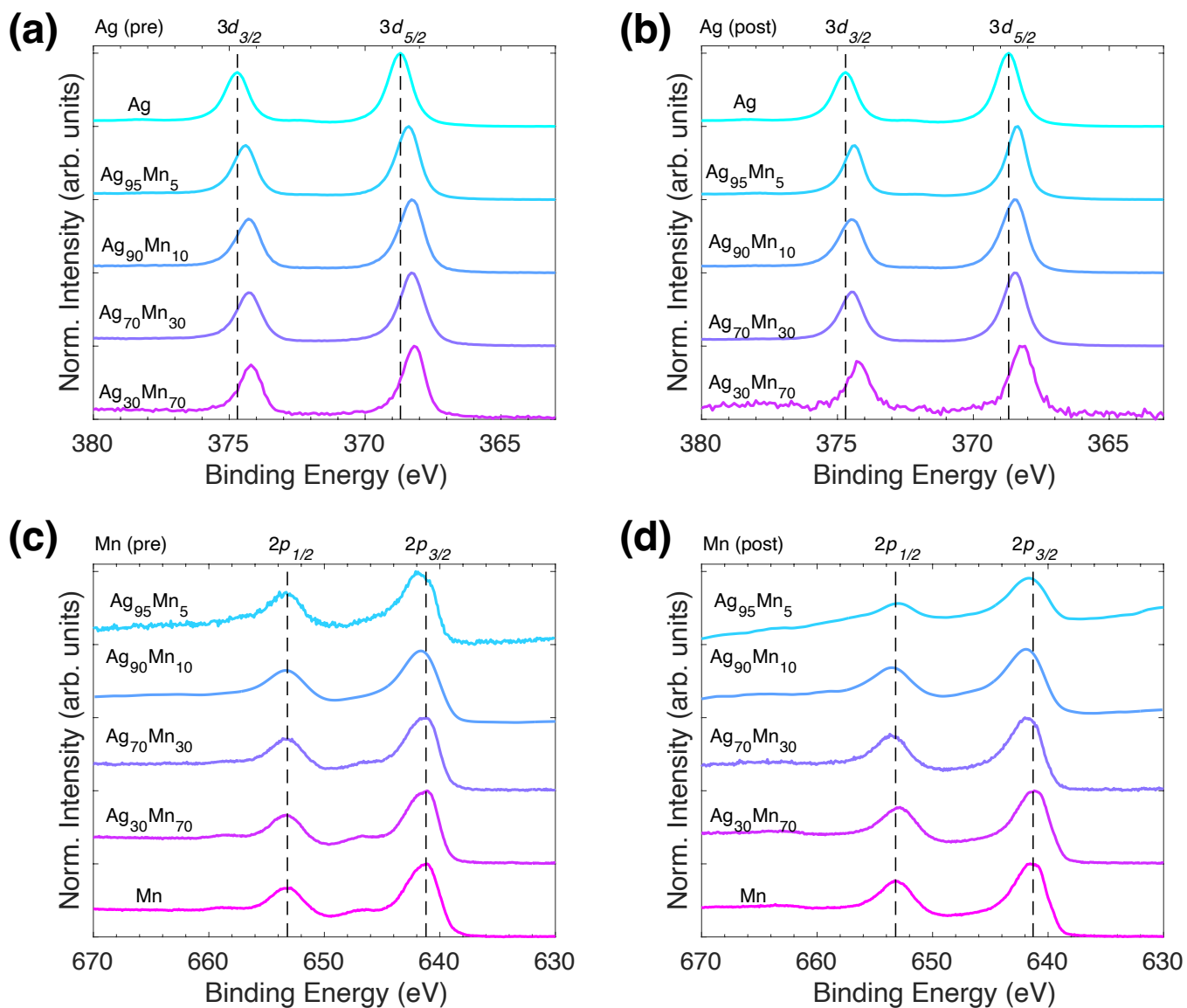


Figure S1. HR (a,b) Ag 3d and (c,d) Mn 2p XPS spectra of Ag_xMn_{1-x} before (a,c) and after (b,d) ORR testing.

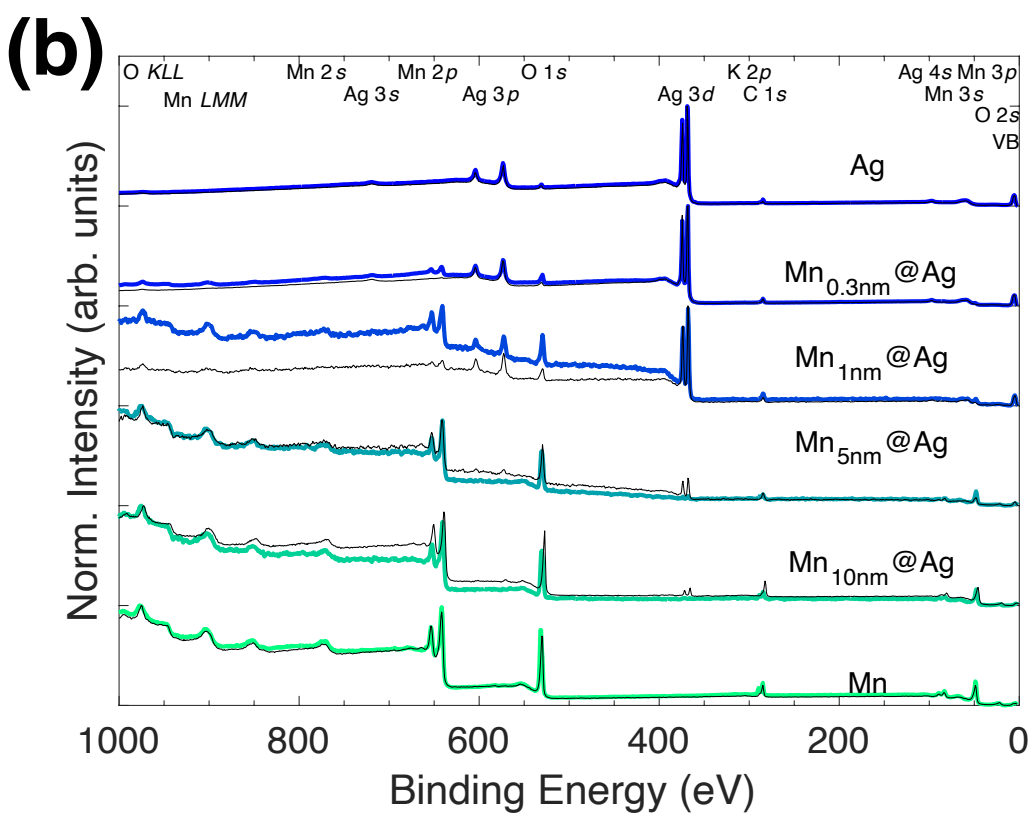
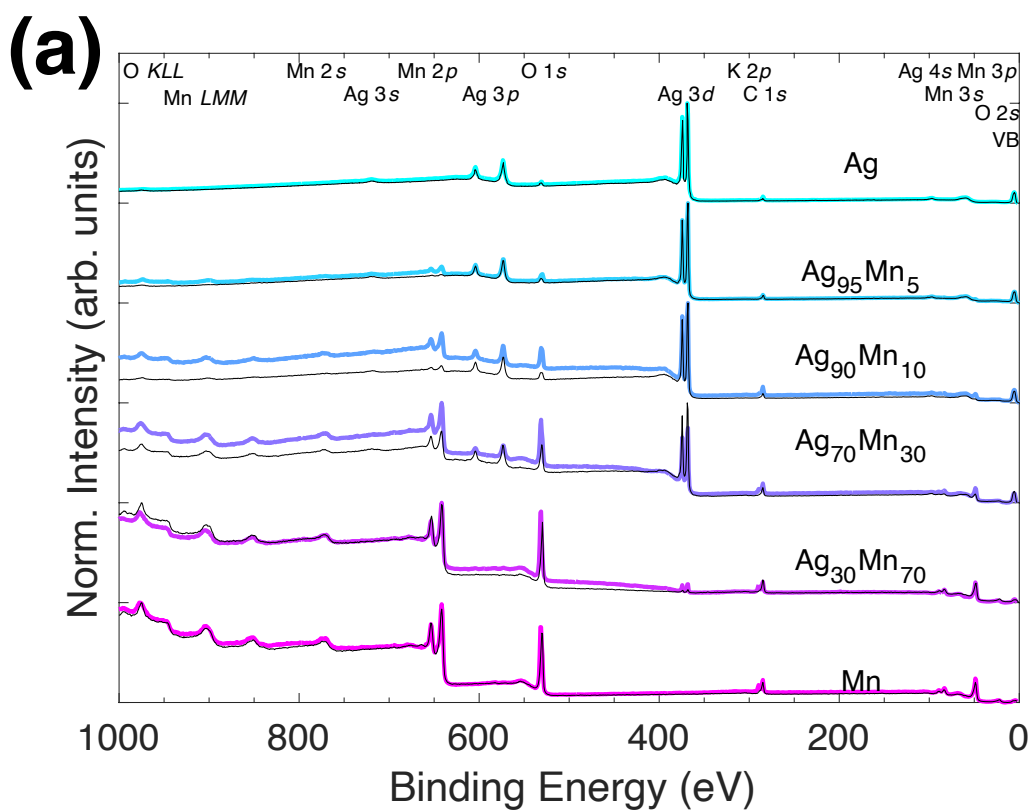


Figure S2. Survey XPS spectra of (a) $\text{Ag}_x\text{Mn}_{1-x}$ and (b) $\text{Mn}_y@Ag_{70\text{nm}-y}$ before (colored lines) and after (black lines) ORR testing (post 20 CVs in O_2 + 2 CVs in N_2 , 20 mV s^{-1} at 1600 rpm).

Table S1. Ag/Mn quantification (representative from Su and HR XPS) and Mn-oxide species compositional analysis from fitted (see examples in **Supplementary Figure S4**) HR XPS Mn $2p_{3/2}$ spectra of Ag_xMn_{1-x} before and after ORR testing. The average valency shown is **Figure 2c** is average based on the oxidation state composition of the Mn $2p_{3/2}$ fit in this table: Avg. Mn Valency = $2 \cdot (Mn^{2+}\%) + 2.835 \cdot (Mn^{2.835+}\%) + 4 \cdot (Mn^{4+}\%)$. The trends in XPS composition and oxidation/valency are reliable; however, the absolute values have a possible intrinsic technique error of at least ~ 10 at%.¹ It is standard for XPS metal peaks (i.e. Ag) to be analyzed via Tougaard background correction, while XPS peaks for oxides (i.e. $Mn^{>0+}$) are generally analyzed with a Shirley background correction.¹ However, for the purposes of comparison between relative Ag-Mn elemental compositions a Tougaard background correction was employed. Because this is not ideal for Mn there is some added systematic error in the absolute values of Ag:Mn composition.¹ Considering the intrinsic technique/analysis error, plus select duplicate or triplicate measurements (on both the same and/or separate samples) of some Ag_xMn_{1-x} thin films, we observe errors from ± 5 -20 at% for Ag, Mn, and Mn-oxide fit compositions. For Mn $2p_{3/2}$ peak fitting, a Shirley background correction was employed.

	pre							post						
	Quant.		HR Mn $2p_{3/2}$ Fit					Mn 3s Splitting (eV)	Quant.		HR Mn $2p_{3/2}$ Fit			
Ag	Mn	MnO (Mn ²⁺) (at%)	Mn ₂ O ₃ (Mn ³⁺) + Mn ₃ O ₄ (Mn ^{2.67+}) (Mn ^{2.835+}) (at%)	MnO ₂ (Mn ⁴⁺) (at%)	Avg. Mn Valency	Ag	Mn		MnO (Mn ²⁺) (at%)	Mn ₂ O ₃ (Mn ³⁺) + Mn ₃ O ₄ (Mn ^{2.67+}) (Mn ^{2.835+}) (at%)	MnO ₂ (Mn ⁴⁺) (at%)	Avg. Mn Valency	Mn 3s Splitting (eV)	
Mn	0	100	75	22	3	2.2	5.9	0	100	34	31	35	3.0	5.6
Ag ₃₀ Mn ₇₀	5	95	60	29	11	2.5	5.9	2	98	38	20	42	3.0	5.5
Ag ₇₀ Mn ₃₀	36	64	59	28	13	2.5	5.9	59	41	23	41	36	3.1	5.6
Ag ₉₀ Mn ₁₀	60	40	57	23	20	2.6	5.8	88	12	28	49	23	2.9	5.5
Ag ₉₅ Mn ₅	84	16	53	29	19	2.6	5.7	97	3	24	45	30	3.0	No signal
Ag	100	0	N/A	N/A	N/A	N/A	N/A	100	0	N/A	N/A	N/A	N/A	N/A

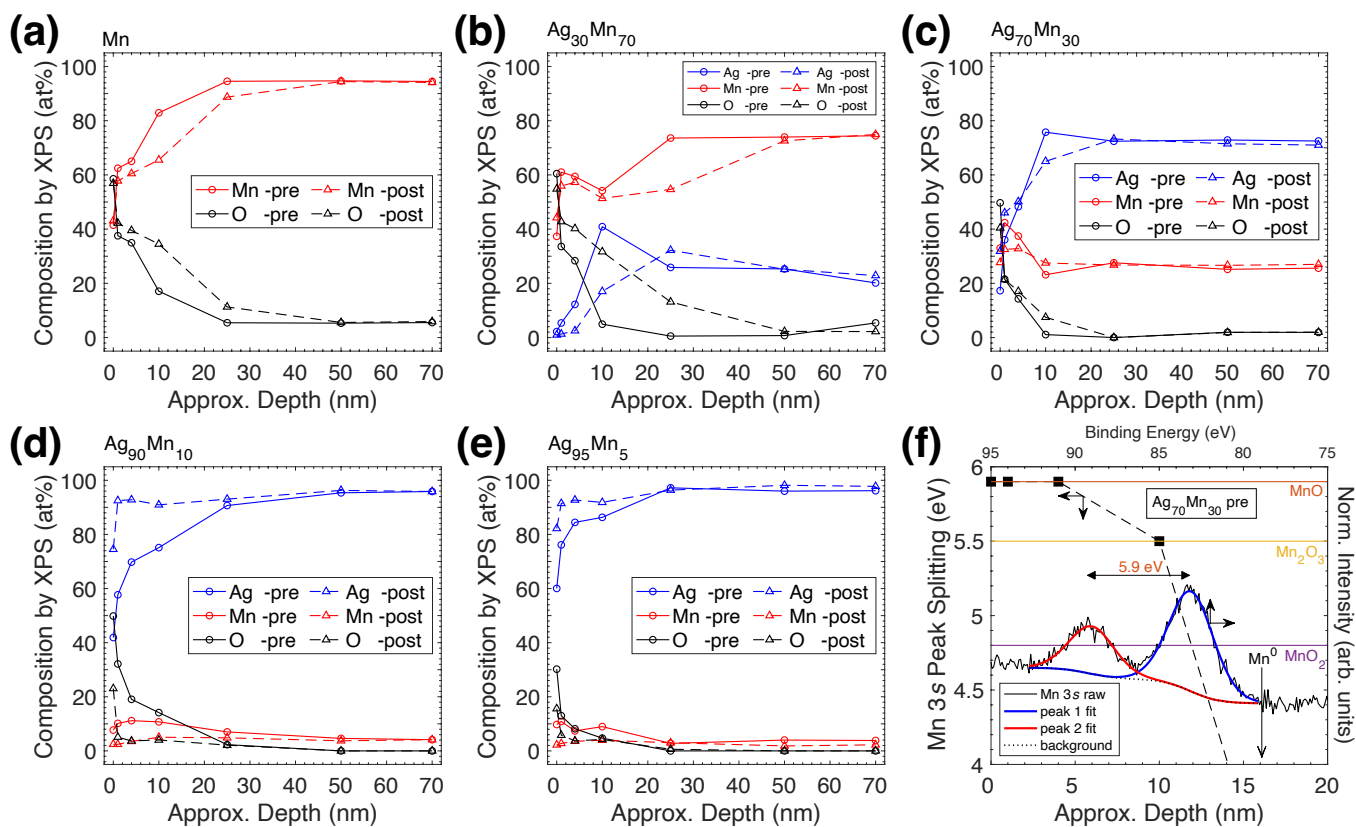


Figure S3. Representative Ag, Mn, and O content by survey XPS depth profiling (Ar^+ sputtering) before and after ORR testing of (a) Mn, (b) $\text{Ag}_{30}\text{Mn}_{70}$, (c) $\text{Ag}_{70}\text{Mn}_{30}$, (d) $\text{Ag}_{90}\text{Mn}_{10}$, and (e) $\text{Ag}_{95}\text{Mn}_5$ as a function of the approximated cumulative sputtered depth (calibrated to SiO_2 sputtering as provided the SNSF facility). (f) Representative, select, Mn 3s peak splitting separation (left and top axes) of $\text{Ag}_{70}\text{Mn}_{30}$ pre-ORR testing as a function of the approximated cumulative sputtered depth and the corresponding fitted Mn 3s spectra (right and top axes) before sputtering (0 nm), which is in this case representative of a 2^+ oxidation state (MnO).² A Mn 3s peak splitting of ~ 5.9 corresponds to MnO , of ~ 5.5 corresponds to Mn_2O_3 , and of ~ 4.8 corresponds to MnO_2 ; the absence of peak splitting suggests a metallic Mn^0 oxidation state.² The Mn 3s peak splitting in MnO_x is attributed to the coupling of non-ionized 3s electron with 3d valence band electrons.²

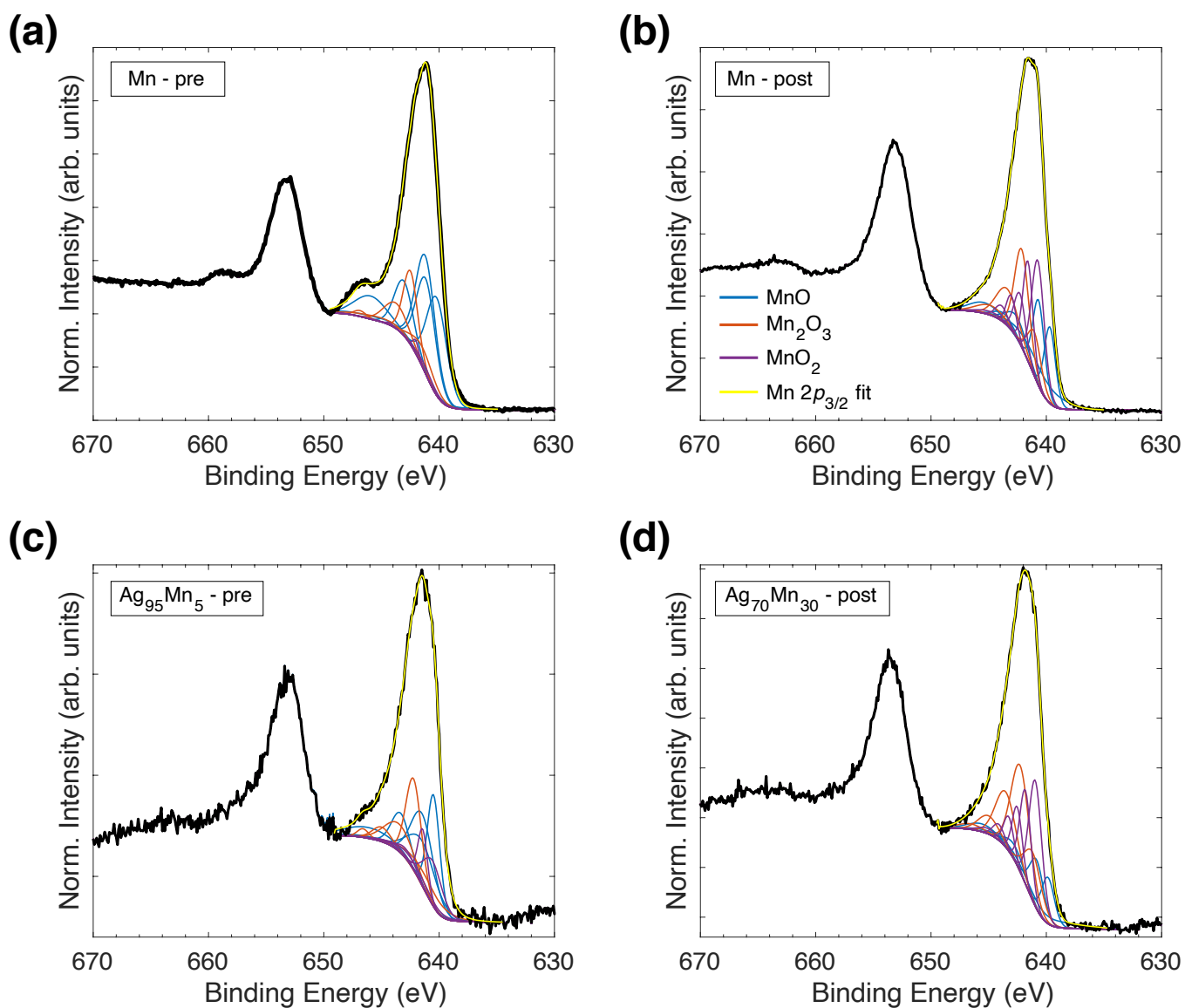


Figure S4. Representative Mn $2p_{3/2}$ fits of select HR XPS spectra of $\text{Ag}_x\text{Mn}_{1-x}$ before and after ORR testing. The Mn $2p_{3/2}$ peaks, with a Shirley background correction, were fitted according to guidelines and initial peak separation ranges, full width half maxima (FWHM), and peak area ratios constraints reported before;² the FWHM was allowed to relaxed to achieve a good fit.

Table S2. Segregation energies (eV) evaluated on metallic $\text{Ag}_x\text{Mn}_{1-x}$ unit cells.

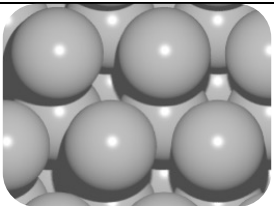
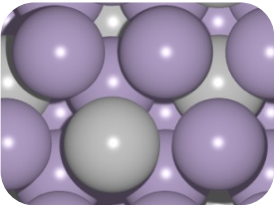
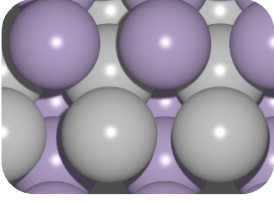
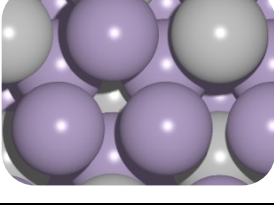
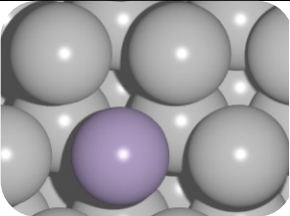
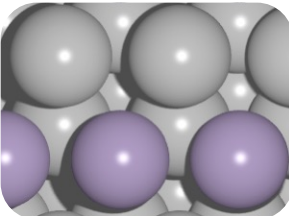
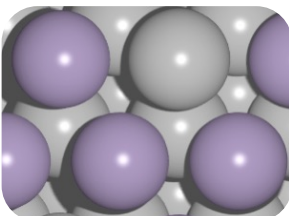
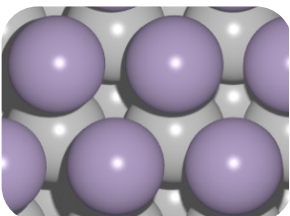
Surface prior to segregation	Segregation energy (eV)		
	vacuum	*OH adsorbed	*O adsorbed
$\text{Ag}_{100}\text{Mn}_0(111)$ 	0.28	-1.21	-1.44
$\text{Ag}_{75}\text{Mn}_{25}(111)$ 	0.29	-0.19	-0.75
$\text{Ag}_{50}\text{Mn}_{50}(111)$ 	0.50	-0.33	-0.81
$\text{Ag}_{25}\text{Mn}_{75}(111)$ 	0.12	-0.28	-1.61

Table S3. Average segregation energies (eV) evaluated on a Ag(111) surface at dilute Mn conditions. Average segregation energies were calculated using, $E_{\text{seg}} = [nMn_{\text{surface-Ag(111)}} + (n-1) * Ag(111) - n * 1Mn_{\text{bulk-Ag(111)}}]/n$ where $Mn_{\text{surface-Ag(111)}}$, $Ag(111)$, and $Mn_{\text{bulk-Ag(111)}}$ are VASP calculated electronic energies of the Ag unit cell with Mn on surface site, pristine Ag unit cell, and Ag unit cell with Mn on bulk site. n is the number of Mn atoms present in the system.

Surface upon segregation		Segregation Energy (eV)		
		vacuum	*OH adsorbed	*O adsorbed
1Mn _{surface-Ag(111)}		0.28	-1.21	-1.44
2Mn _{surface-Ag(111)}		0.32	-0.41	-0.51
3Mn _{surface-Ag(111)}		0.36	-0.13	-0.76
4Mn _{surface-Ag(111)}		0.37	0.00	-0.02

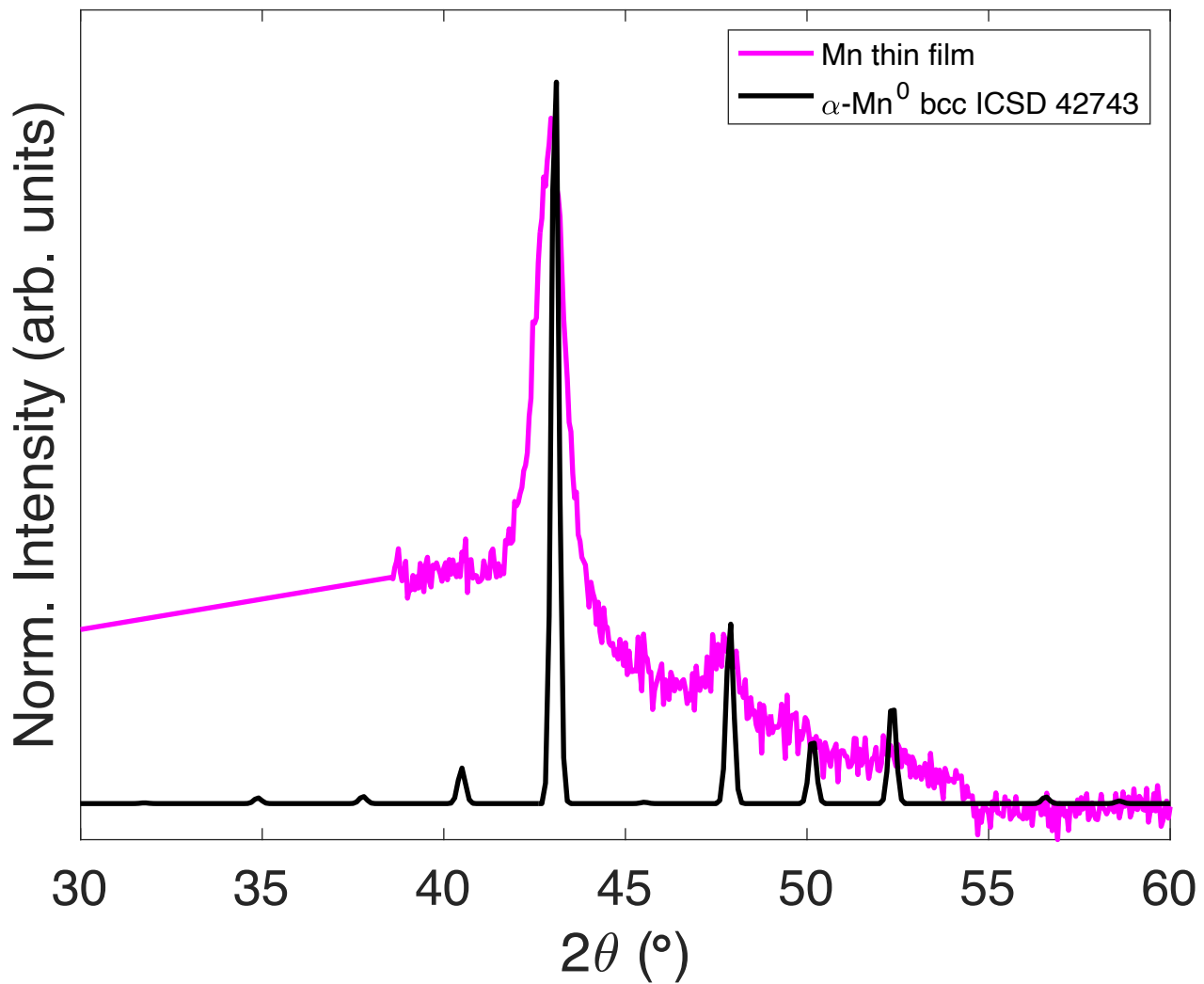


Figure S5. Background-subtracted Mn thin film GI-XRD (magenta) overlaid with the reference (ICSD 42743) α -Mn (metal) bcc diffractogram (black).

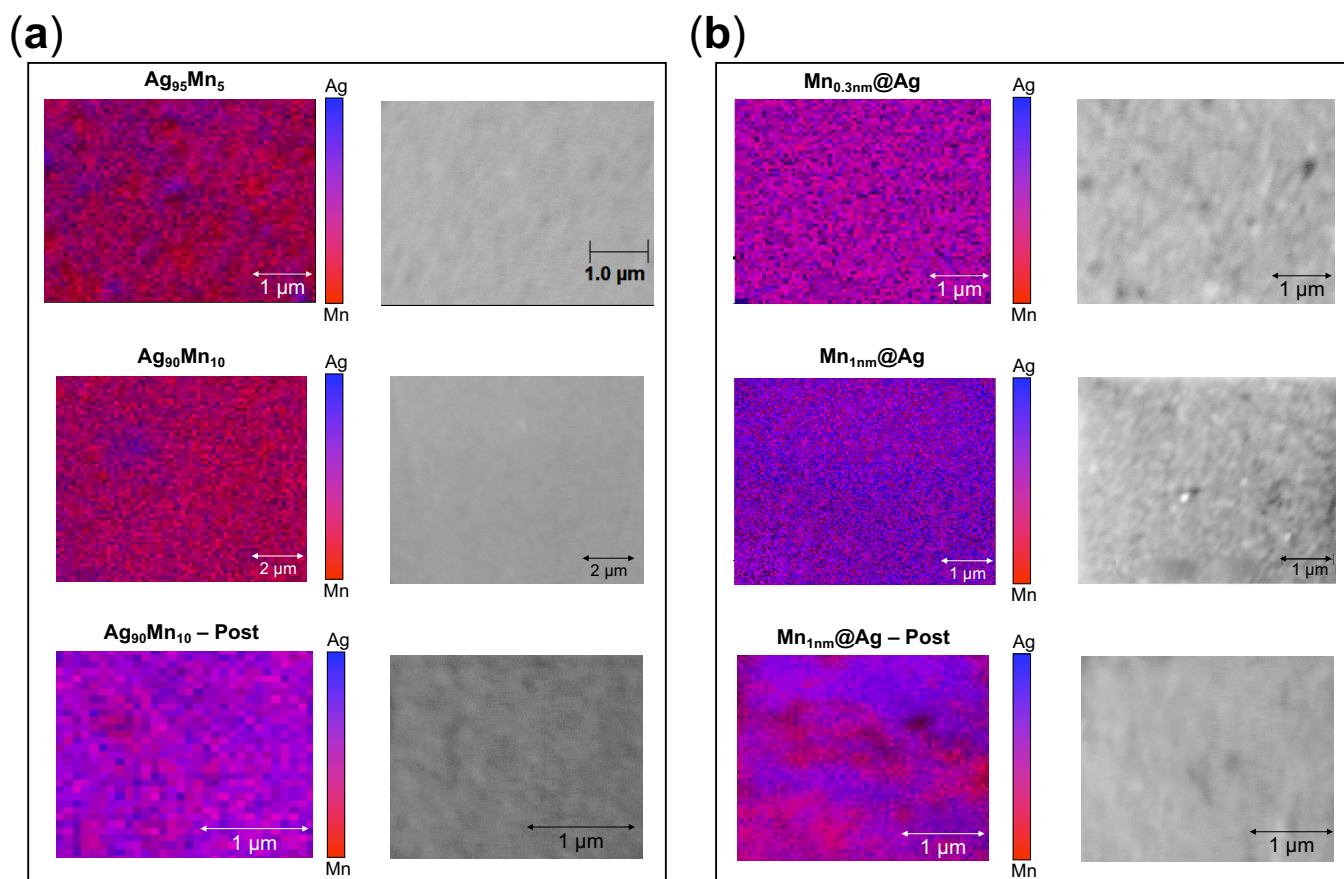


Figure S6. Auger electron spectroscopy (AES) near-surface overlaid Ag (blue) and Mn (red) mapping, with corresponding SEM image (secondary electron detector) of mapped area, of select Ag-Mn samples: **(a)** as-deposited $\text{Ag}_{95}\text{Mn}_5$, as-deposited $\text{Ag}_{90}\text{Mn}_{10}$ and post-ORR testing $\text{Ag}_{90}\text{Mn}_{10}$ on the left column and **(b)** as-deposited $\text{Mn}_{0.3\text{nm}}@\text{Ag}$, as-deposited $\text{Mn}_{1\text{nm}}@\text{Ag}$ and post-ORR testing $\text{Mn}_{1\text{nm}}@\text{Ag}$ on the right column. The color bars have arbitrary units and the RGB color magnitudes displayed are relative to each individual map, and thus qualitative when comparing Ag and Mn compositions. The texture in the SEM images is attributed to the crystallite grain boundaries of the film and has been seen before on polycrystalline films.³ Measurements were taken 2 to 4 weeks after synthesis (for the as-deposited samples) or after electrochemical testing (for the post-ORR samples). Raw data was overlaid and plotted with Multipack (PHI company software).

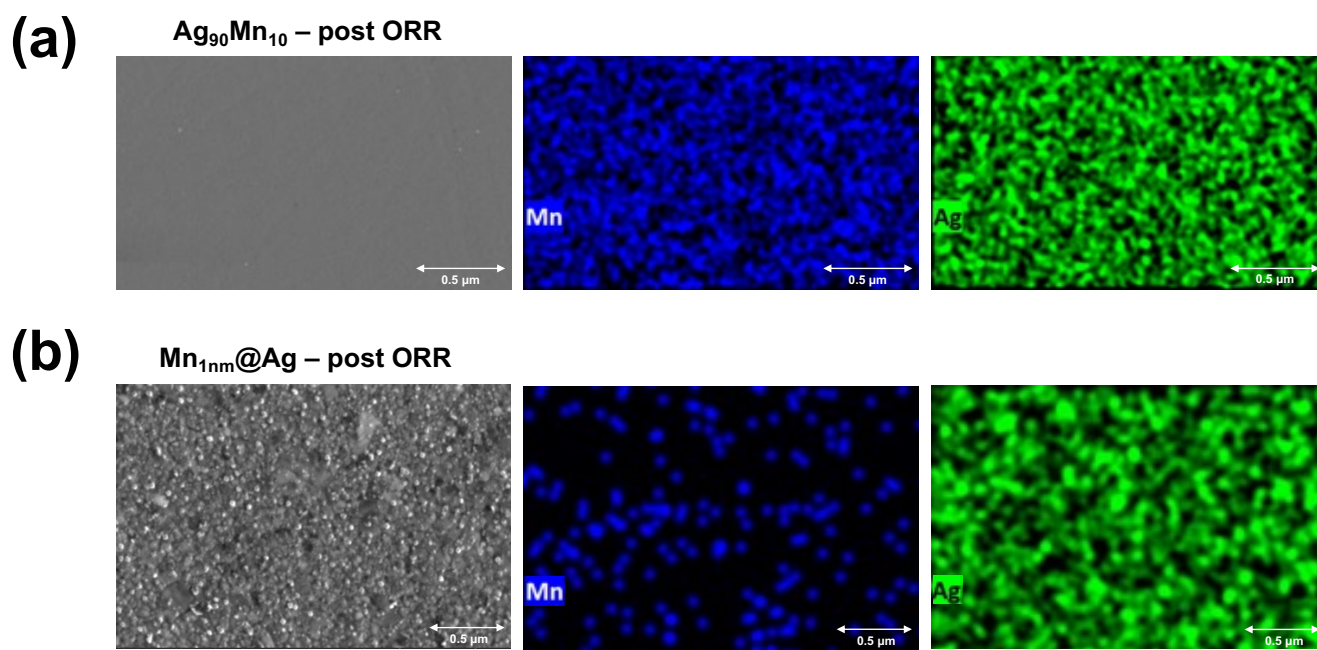
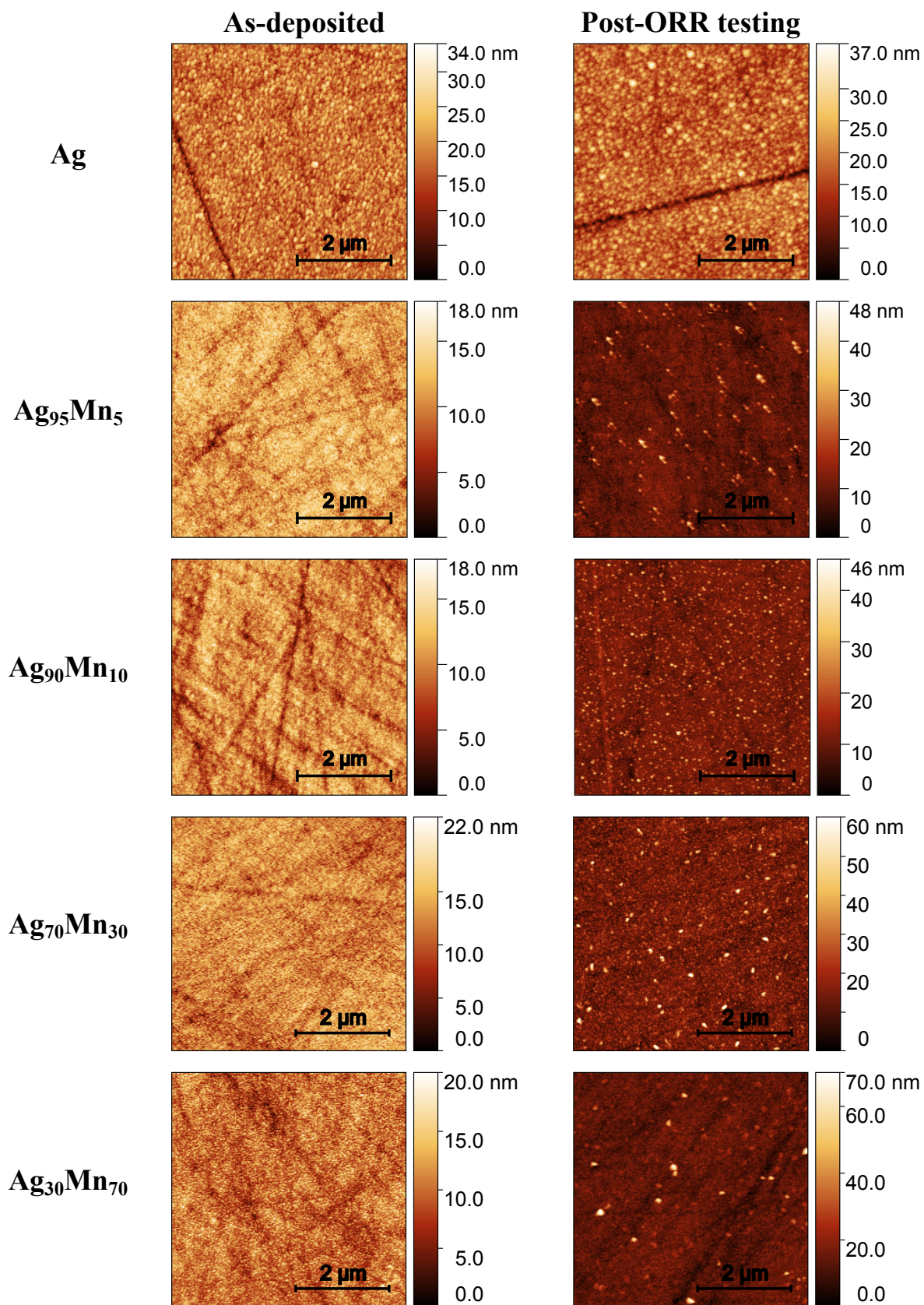


Figure S7. Scanning electron microscopy (SEM, ETD detector) and energy dispersive X-ray spectroscopy (EDS) bulk Mn (blue) and Ag (green) mapping of select Ag-Mn samples: **(a)** $\text{Ag}_{90}\text{Mn}_{10}$ post-ORR, and **(b)** $\text{Mn}_{1\text{nm}}\text{@Ag}$ post-ORR. The color intensity has arbitrary units and is relative to each individual map, and thus qualitative when comparing Ag and Mn compositions to each other. The background texture in the SEM images taken with a ETD detector (left column) is attributed to the crystallite grain boundaries of the film and has been seen before on polycrystalline films.³ The bright white circular features in the SEM image shown in **(b)** are hypothesized to be MnO_x nano-islands (as suggested by AES mapping; see **Supplementary Figs. S21,S22** and **Note S1**); however, EDS cannot resolve them as the technique in our instrument has approximately a $1\ \mu\text{m} \times 1\ \mu\text{m} \times 1\ \mu\text{m}$ resolution (the Mn signal in **(b)** is mostly background noise). Measurements were taken 2 to 4 weeks after electrochemical testing (for the post-ORR samples). Raw EDS data was processed and plotted with Bruker’s ESPRIT software, and subsequently edited in MS Power Point to crop out instrument artifacts on the borders of the map. Electron beam settings: 20 kV and 1.6 nA. Given that SEM-EDS is a bulk technique, and that the bulk of our thin films remains approximately the same before and after ORR, as measured by XPS depth profiling (**Fig. 2d** and **Fig. S3**), post-ORR SEM-EDS elemental mapping is nominally representative of the films’ bulk both before and after ORR. See more SEM on **Figs. S17–S19**. See extended SEM discussion in **Note S3**.



(Figure S8. Continues on next page)

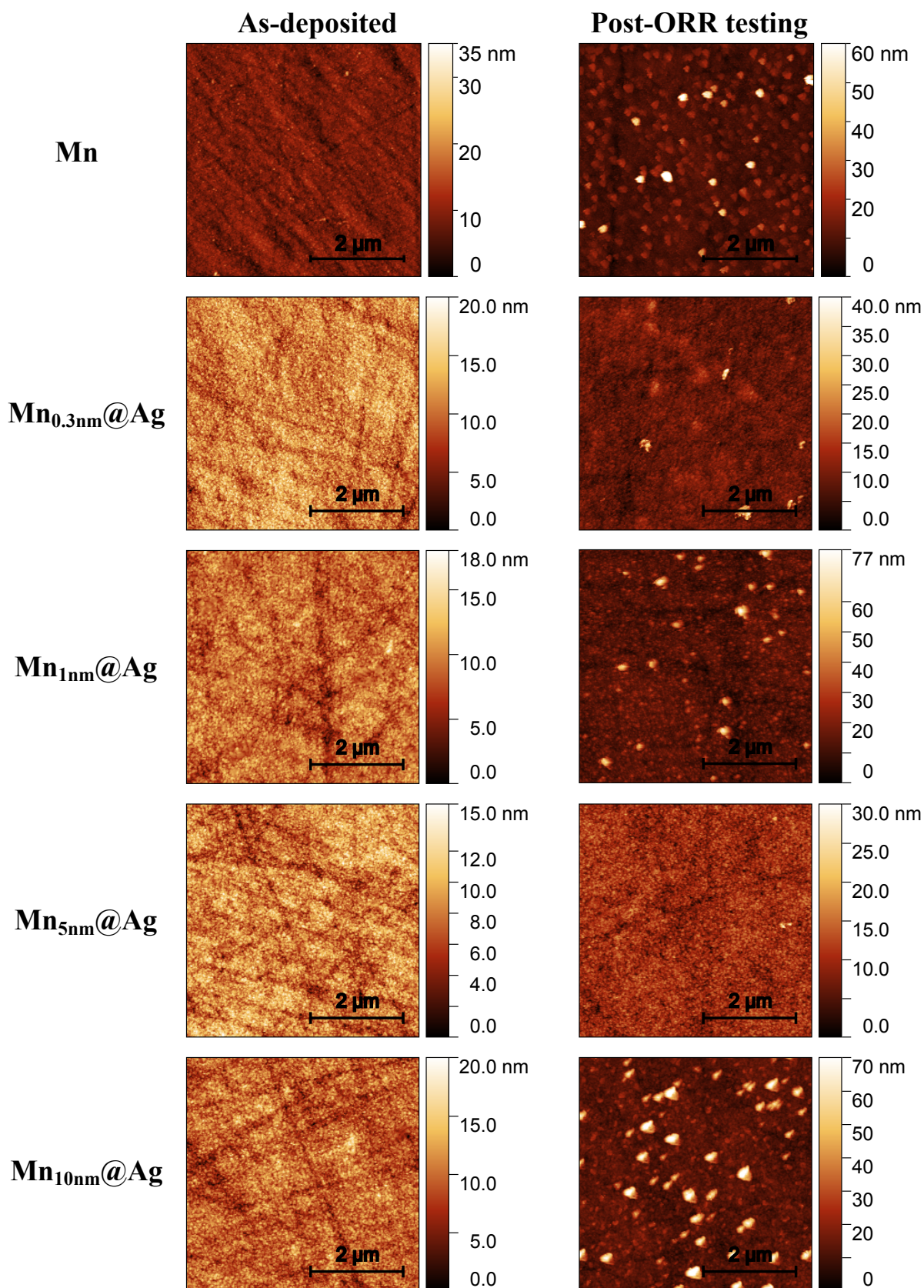


Figure S8. Representative AFM topography images of the $\text{Ag}_x\text{Mn}_{1-x}$ and $\text{Mn}_y@\text{Ag}_{70-y}$ thin films before and after (post 20 CVs in O_2 + 2 CVs in N_2 , 20 mV s^{-1} at 1600 rpm) ORR testing. See roughness metrics in **Supplementary Table S4**.

Table S4. Average roughness factor (RF) and root mean squared roughness (RMSR) from AFM topography measurements of $\text{Ag}_x\text{Mn}_{1-x}$ and $\text{Mn}_y@\text{Ag}_{70-y}$ thin films before and after (post 20 CVs in O_2 + 2 CVs in N_2 , 20 mV s^{-1} at 1600 rpm) ORR testing. Averages and standard deviations are based on at least 3 separate measurements of at least $5 \mu\text{m} \times 5 \mu\text{m}$ scan size (both forward and reverse scans). All AFM data was processed with Gwyddion⁴ software.

	as-deposited (AD)				post ORR-testing					
	AVG. RF	RF Std. Dev.	AVG. RMSR (nm)	RMSR Std. Dev. (nm)	AVG. RF	RF Std. Dev.	AVG. RMSR (nm)	RMSR Std. Dev. (nm)	RF increase ($\times\text{RF}_{\text{AD}}$)	RMSR increase ($\times\text{RF}_{\text{AD}}$)
Ag	1.01	0.01	3.65	0.12	1.01	0.01	4.23	0.34	1.0	1.2
Ag₉₅Mn₅	1.01	0.00	2.41	0.17	1.01	0.01	4.31	1.49	1.0	1.8
Ag₉₀Mn₁₀	1.01	0.00	2.65	0.21	1.01	0.01	4.75	1.44	1.0	1.8
Ag₇₀Mn₃₀	1.01	0.01	2.39	0.34	1.04	0.02	5.73	0.21	1.0	2.4
Ag₃₀Mn₇₀	1.01	0.00	2.80	0.49	1.02	0.02	5.99	2.33	1.0	2.1
Mn	1.01	0.00	4.65	4.77	1.01	0.01	9.19	5.34	1.0	2.0
Mn_{0.3nm}@Ag	1.00	0.00	2.94	0.65	1.01	0.00	5.44	5.34	1.0	1.9
Mn_{1nm}@Ag	1.03	0.00	3.51	0.13	1.04	0.05	6.17	1.13	1.0	1.8
Mn_{5nm}@Ag	1.01	0.00	2.87	1.14	1.01	0.01	3.39	0.94	1.0	1.2
Mn_{10nm}@Ag	1.01	0.00	4.72	1.14	1.01	0.01	7.69	2.82	1.0	1.6

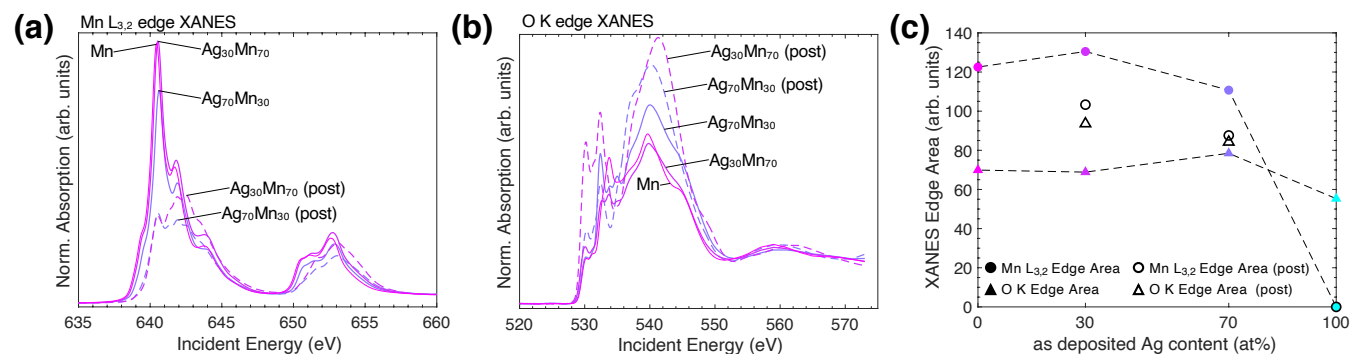


Figure S9. Mn $L_{3,2}$ and O K XANES spectra of select $\text{Ag}_x\text{Mn}_{1-x}$ thin films. Post-ORR spectra collected only for the $\text{Ag}_{70}\text{Mn}_{30}$ and $\text{Ag}_{30}\text{Mn}_{70}$ thin films. Mn $L_{3,2}$ and O K XANES edge area before and after ORR-testing of select $\text{Ag}_x\text{Mn}_{1-x}$ thin films. All XAS data was processed and edge-jump normalized using Larch⁵ software. The area under each curve was calculated by trapezoidal integration using Matlab. Referencing to previously measured spectra of Mn oxide reference standards,⁶ the Mn $L_{3,2}$ XANES spectra shape of Mn, $\text{Ag}_{30}\text{Mn}_{70}$ and $\text{Ag}_{70}\text{Mn}_{30}$ are indicative of MnO , suggesting a dominant Mn^{2+} oxidation state,⁶ in agreement with the HR XPS measurements (**Supplementary Figure S1-S4,S10** and **Table S1,S5**). The similarity in peak areas for Mn and $\text{Ag}_{30}\text{Mn}_{70}$ is attributed to the Mn-enrichment of the near-surface in the mixed $\text{Ag}_{30}\text{Mn}_{70}$ film, reaching a near-surface composition of $\sim 5:95 \text{ Ag}:\text{MnO}_x$, as shown in **Figure 2e**. In addition to limited synchrotron availability, we only performed XANES on $\text{Ag}_{70}\text{Mn}_{30}$ and $\text{Ag}_{30}\text{Mn}_{70}$ because, as explained throughout the main text, they are representative of the Ag-rich and Mn-rich compositional-activity motifs, respectively.

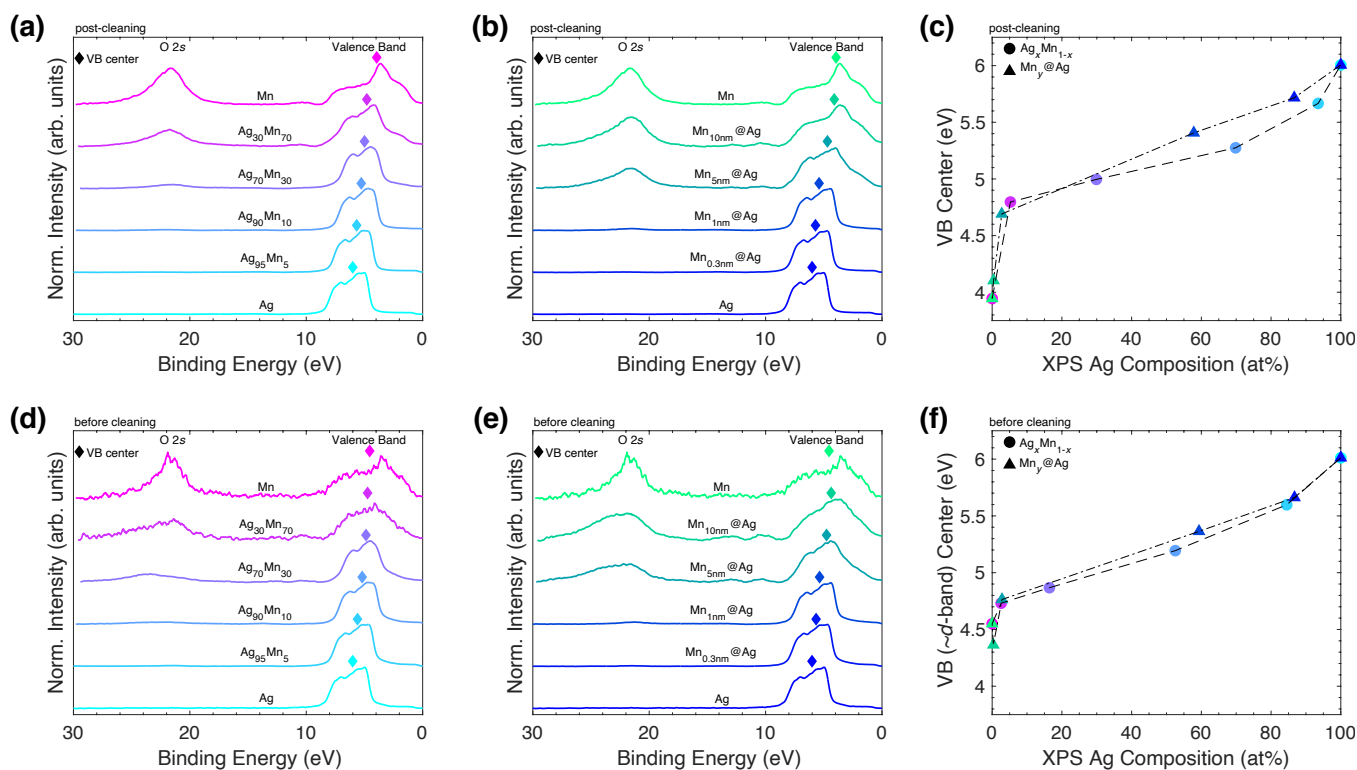


Figure S10. Representative valence band (VB) XPS after Ar^+ sputtering cleaning of the as-deposited (air-exposed) (a) $\text{Ag}_x\text{Mn}_{1-x}$ and (b) $\text{Mn}_y@Ag$ thin films with their corresponding (c) VB-center (weighted mean-energy) as a function of XPS Ag content (also shown in a,b as diamonds). Representative valence band (VB) XPS before sample cleaning of the (d) $\text{Ag}_x\text{Mn}_{1-x}$ and (e) $\text{Mn}_y@Ag$ thin films with their corresponding (f) VB-center (weighted mean-energy) as a function of XPS Ag content (also shown in a,b as diamonds). VB XPS collected at 20 eV pass energy, with 0.05 eV energy steps and 50 ms dwell time. In general Ar^+ sputtering cleaning of the samples resulted in small Ag:Mn compositional changes and negligible changes in overall Mn oxidation state, while significantly improving the VB resolution owing to the removal of convoluting adventitious carbonaceous contamination (see **Supplementary Table S5**). VB XPS was collected on samples grown on Si(111) wafers for ease of measurement and to be able to make electrical contact to the samples from the surface with mounting clips and avoid use of the neutralizer. See more details in **Supplementary Table S5**.

Table S5. Summary of representative valence band (VB) and complementary HR and Su XPS results of the $\text{Ag}_x\text{Mn}_{1-x}$ and $\text{Mn}_y@\text{Ag}$ thin films before and after Ar^+ sputtering cleaning. To calculate VB-band center and normalized areas, the spectra were divided into the VB-region $\sim 0\text{--}15$ eV and the entire collected BE range region up to 30 eV (which includes the O 2s peak) and the maximum intensity was set to 1 arb. unit. The role the O 2s in adsorbate bonding is unclear, while the O 2p contributes to the VB region ($\sim 0\text{--}15$ eV). For completeness, we provide the VB-area and VB-center from both $\sim 0\text{--}14$ eV and $0\text{--}30$ eV. We use Matlab trapezoidal integration to calculate the normalized VB-area and define the VB-center as the as a weighted mean energy of the spectrum⁵ in the BE range of interest.

	sample	Su Quant.		HR Mn $2p_{3/2}$ Fit			Mn 3s splitting (eV)	VB area center (eV)	VB norm. integrated area (arb. units)	VB area center with O 2s (eV)	VB norm. integrated area with O 2s (arb. units)
		Ag (at%)	Mn (at%)	MnO (%)	$\text{Mn}_2\text{O}_3 + \text{Mn}_3\text{O}_4$ (%)	MnO_2 (%)					
post Ar^+ cleaning	Mn	0	100	69	20	11	5.88	3.94	3.82	7.52	7.11
	$\text{Ag}_{30}\text{Mn}_{70}$	5	95	75	14	11	5.99	4.80	4.01	5.93	5.75
	$\text{Ag}_{70}\text{Mn}_{30}$	30	70	81	11	8	5.98	5.00	3.45	5.23	3.86
	$\text{Ag}_{90}\text{Mn}_{10}$	70	30	71	26	3	5.85	5.27	3.27	5.31	3.33
	$\text{Ag}_{95}\text{Mn}_5$	94	7	37	43	20	no signal	5.67	3.22	5.69	3.26
	Ag	100	0	N/A	N/A	N/A	N/A	6.01	3.19	6.03	3.24
	$\text{Mn}_{0.3\text{nm}}@\text{Ag}$	87	13	50	28	22	no signal	5.72	3.26	5.73	3.29
	$\text{Mn}_{1\text{nm}}@\text{Ag}$	58	42	58	26	16	5.64	5.41	3.40	5.50	3.58
	$\text{Mn}_{5\text{nm}}@\text{Ag}$	3	97	75	12	13	5.89	4.69	4.35	6.08	6.53
	$\text{Mn}_{10\text{nm}}@\text{Ag}$	0	100	77	4	19	5.89	4.10	4.61	6.49	7.69
before sample cleaning	Mn	0	100	68	20	12	5.95	4.55	4.35	7.95	7.67
	$\text{Ag}_{30}\text{Mn}_{70}$	3	97	81	12	7	6.00	4.73	4.00	6.97	6.72
	$\text{Ag}_{70}\text{Mn}_{30}$	16	84	70	22	8	5.86	4.87	3.43	5.52	4.53
	$\text{Ag}_{90}\text{Mn}_{10}$	53	47	58	22	21	5.83	5.19	3.43	5.38	3.77
	$\text{Ag}_{95}\text{Mn}_5$	85	16	45	26	29	5.69	5.60	3.40	5.64	3.48
	Ag	100	0	N/A	N/A	N/A	N/A	6.01	3.27	6.06	3.36
	$\text{Mn}_{0.3\text{nm}}@\text{Ag}$	87	13	34	32	34	no signal	5.66	3.40	5.67	3.43
	$\text{Mn}_{1\text{nm}}@\text{Ag}$	59	41	56	21	23	5.75	5.36	3.37	5.50	3.60
	$\text{Mn}_{5\text{nm}}@\text{Ag}$	3	97	69	21	11	5.93	4.76	4.24	6.39	6.79
	$\text{Mn}_{10\text{nm}}@\text{Ag}$	0	100	73	17	11	5.90	4.36	4.92	7.05	8.55

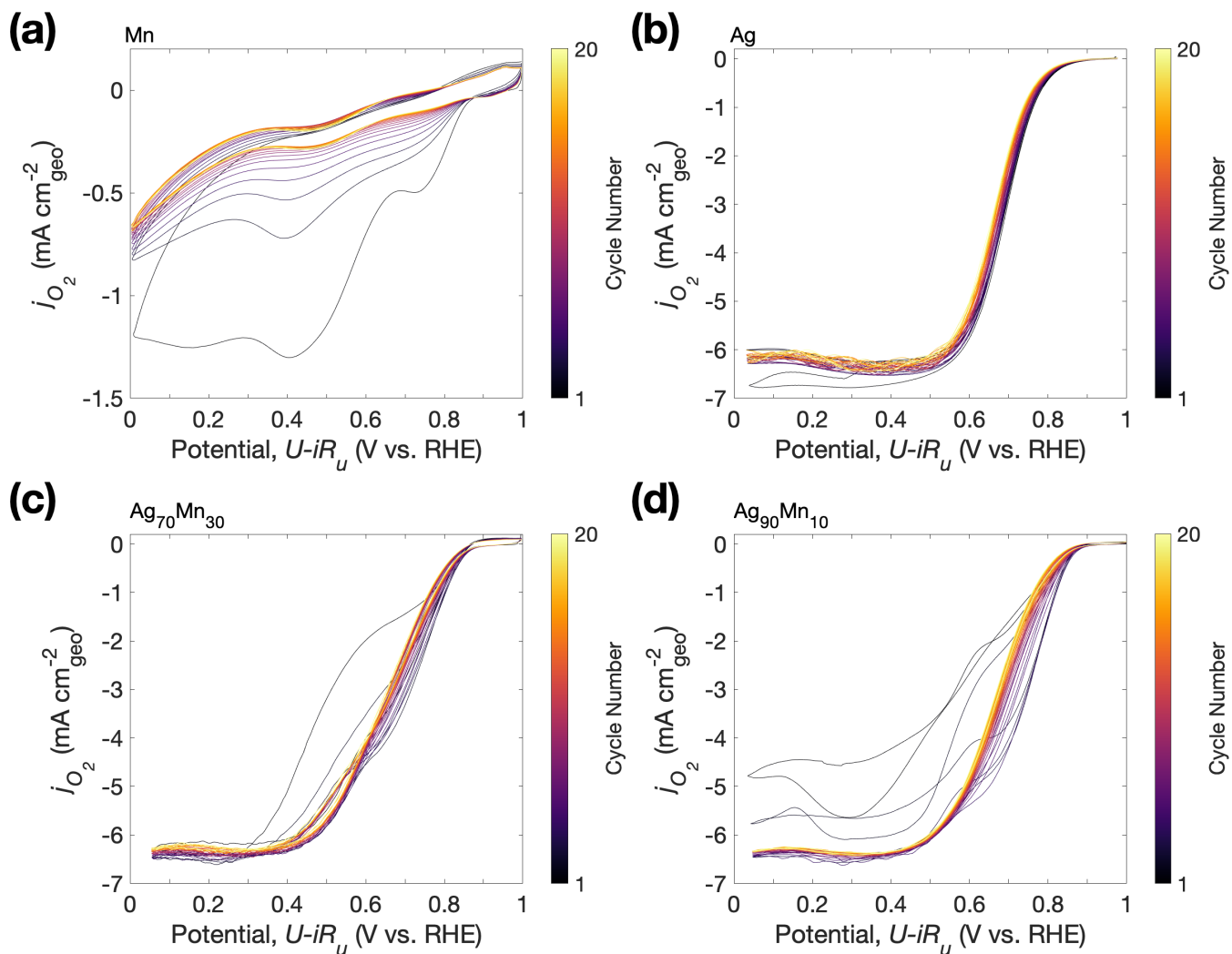


Figure S11. Representative 20 CV cycles in O_2 -saturated 0.1 M KOH for representative (a) Mn, (b) Ag, (c) $Ag_{70}Mn_{30}$, and (d) $Ag_{90}Mn_{10}$ thin films showing.

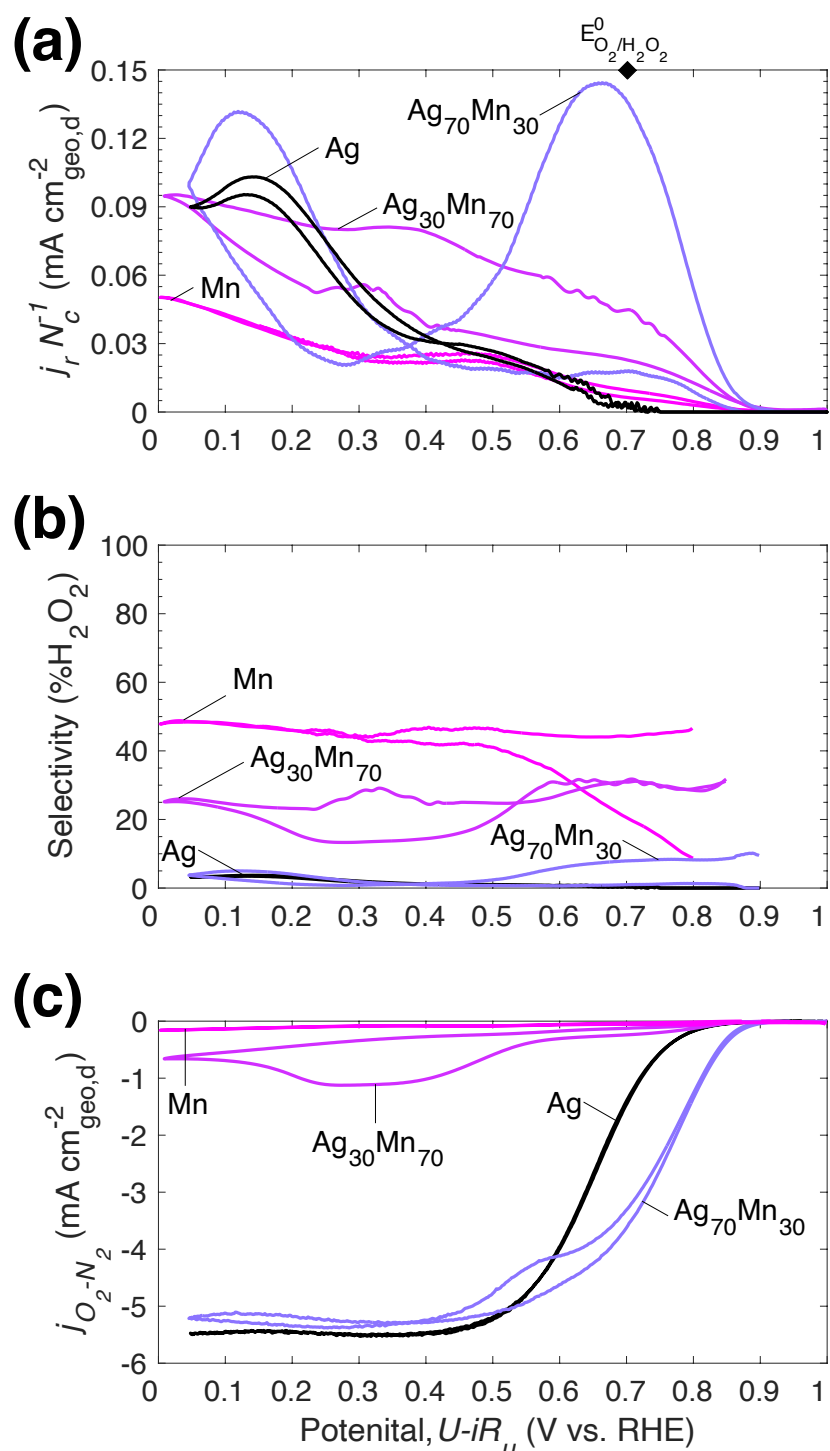


Figure S12. RRDE of select representative Ag_xMn_{1-x} thin films. **(a)** H_2O_2 current density (Pt ring current normalized by the disk (d) geometric area and divided by collection efficiency, $N_c = 0.22$)⁷⁻⁹, **(b)** H_2O_2 selectivity (truncated to slightly above the average onset potential of each film), and **(c)** disk current density (subtracted N_2 CV collected after 20th cycle in O_2) as a function of potential for Ag (3rd CV cycle), $Ag_{70}Mn_{30}$ (4th CV cycle), $Ag_{30}Mn_{70}$ (5th CV cycle), and Mn (20th CV cycle) thin films. Denoted with a diamond is the standard reduction potential of O_2 to H_2O_2 , $E_{O_2/H_2O_2}^0$.⁷⁻⁹ Note that the concentration of H_2O_2 is variable as a function of testing (and not at a chemical activity of 1).⁹ The best performing CV cycles were used for $Ag_{70}Mn_{30}$, $Ag_{30}Mn_{70}$ and the converged/steady state CV cycles were used for Ag and Mn. Performance trends in (c) follow those in RDE shown in the main text (**Figure 2**).

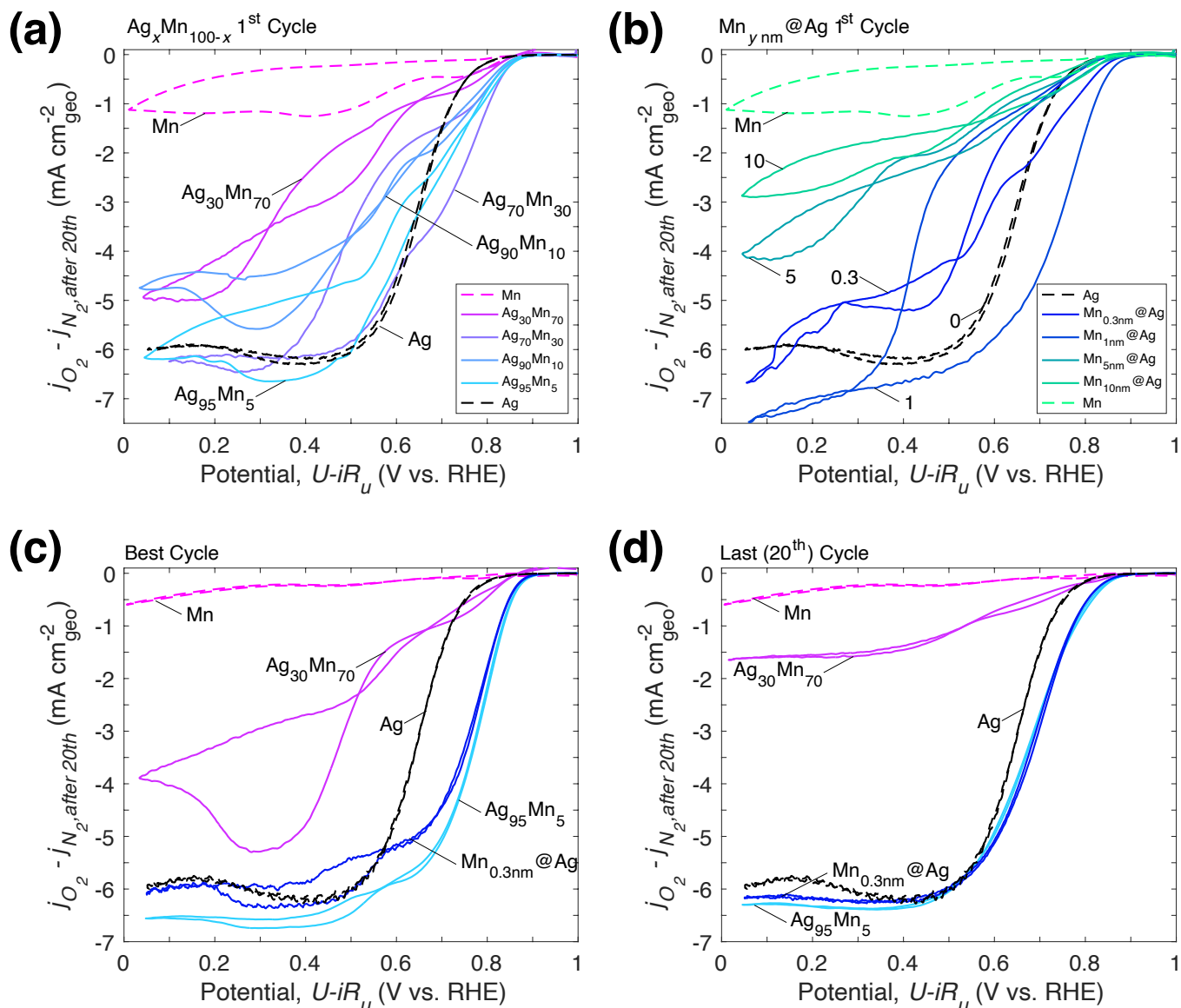


Figure S13. Representative 1st cycle ORR CV for the (a) Ag_xMn_{100-x} and (b) Mn_y@Ag thin films. (c) Best and (d) last (20th) ORR CV cycle comparison between the composition–activity motifs of the Ag_xMn_{100-x} and Mn_y@Ag thin films. For consistency the converged Mn CV (20th cycle) and the 3rd Ag CV cycle are used for comparison in (c-d).

Table S6. Summary of ORR activity metrics at the first, ~best, and final (20th) cycle for Ag_xMn_{1-x} and Mn_y@Ag. Average (AVG) and standard deviation (STDEV) from at least triplicate measurements (with separate samples and electrolyte). Specific activity or kinetic current density, j_k , at 0.8 V_{RHE} is based on the average AFM-measured (Supplementary Table S4) exposed catalyst surface area measured after ORR testing (20 O₂ CVs + 2 N₂ CVs). Note that these metrics do not necessarily account for the complete overall CV performance for Ag₃₀Mn₇₀, Mn_{5nm}@Ag, and Mn_{10nm}@Ag, which overall perform worse than Ag (Figure 3, 5 and Supplementary Figure S13).

cycle	sample	AVG onset potential (V _{RHE}) at -0.1 mA cm _{geo} ⁻²	STDEV onset potential (V _{RHE}) at -0.1 mA cm _{geo} ⁻²	AVG $j_{k,0.8V_{RHE}}$ (mA cm _{AFM} ⁻²)	STDEV $j_{k,0.8V_{RHE}}$ (mA cm _{AFM} ⁻²)	AVG Tafel slope (mV dec ⁻¹)	STEDEV Tafel slope (mV dec ⁻¹)
20	Mn	0.67	0.04	-0.1	0.0	122	10
3	Ag	0.83	0.01	-0.3	0.1	90	2
1	Ag ₃₀ Mn ₇₀	0.84	0.01	-0.3	0.1	149	30
	Ag ₇₀ Mn ₃₀	0.85	0.02	-0.5	0.4	118	36
	Ag ₉₀ Mn ₁₀	0.86	0.01	-0.8	0.4	70	4
	Ag ₉₅ Mn ₅	0.87	0.03	-0.7	0.2	65	7
~best	Ag ₃₀ Mn ₇₀	0.84	0.01	-0.3	0.1	143	5
	Ag ₇₀ Mn ₃₀	0.87	0.00	-1.5	0.1	55	4
	Ag ₉₀ Mn ₁₀	0.88	0.01	-1.9	0.5	53	3
	Ag ₉₅ Mn ₅	0.88	0.01	-2.7	0.7	51	4
20	Ag ₃₀ Mn ₇₀	0.78	0.04	-0.1	0.1	258	105
	Ag ₇₀ Mn ₃₀	0.87	0.01	-0.8	0.1	89	7
	Ag ₉₀ Mn ₁₀	0.86	0.00	-0.8	0.2	61	4
	Ag ₉₅ Mn ₅	0.86	0.01	-0.8	0.3	58	5
1	Mn _{0.3nm} @Ag	0.85	0.01	-0.5	0.2	78	25
	Mn _{1nm} @Ag	0.86	0.01	-0.9	0.5	91	3
	Mn _{5nm} @Ag	0.85	0.01	-0.4	0.1	97	17
	Mn _{10nm} @Ag	0.84	0.01	-0.5	0.2	99	26
~best	Mn _{0.3nm} @Ag	0.88	0.01	-2.3	0.4	51	3
	Mn _{1nm} @Ag	0.88	0.01	-1.8	0.3	60	7
	Mn _{5nm} @Ag	0.87	0.01	-0.8	0.3	66	5
	Mn _{10nm} @Ag	0.85	0.01	-0.5	0.2	72	6
20	Mn _{0.3nm} @Ag	0.86	0.01	-0.8	0.3	63	5
	Mn _{1nm} @Ag	0.87	0.01	-1.1	0.2	64	4
	Mn _{5nm} @Ag	0.87	0.01	-0.6	0.2	94	8
	Mn _{10nm} @Ag	0.84	0.01	-0.3	0.1	147	52

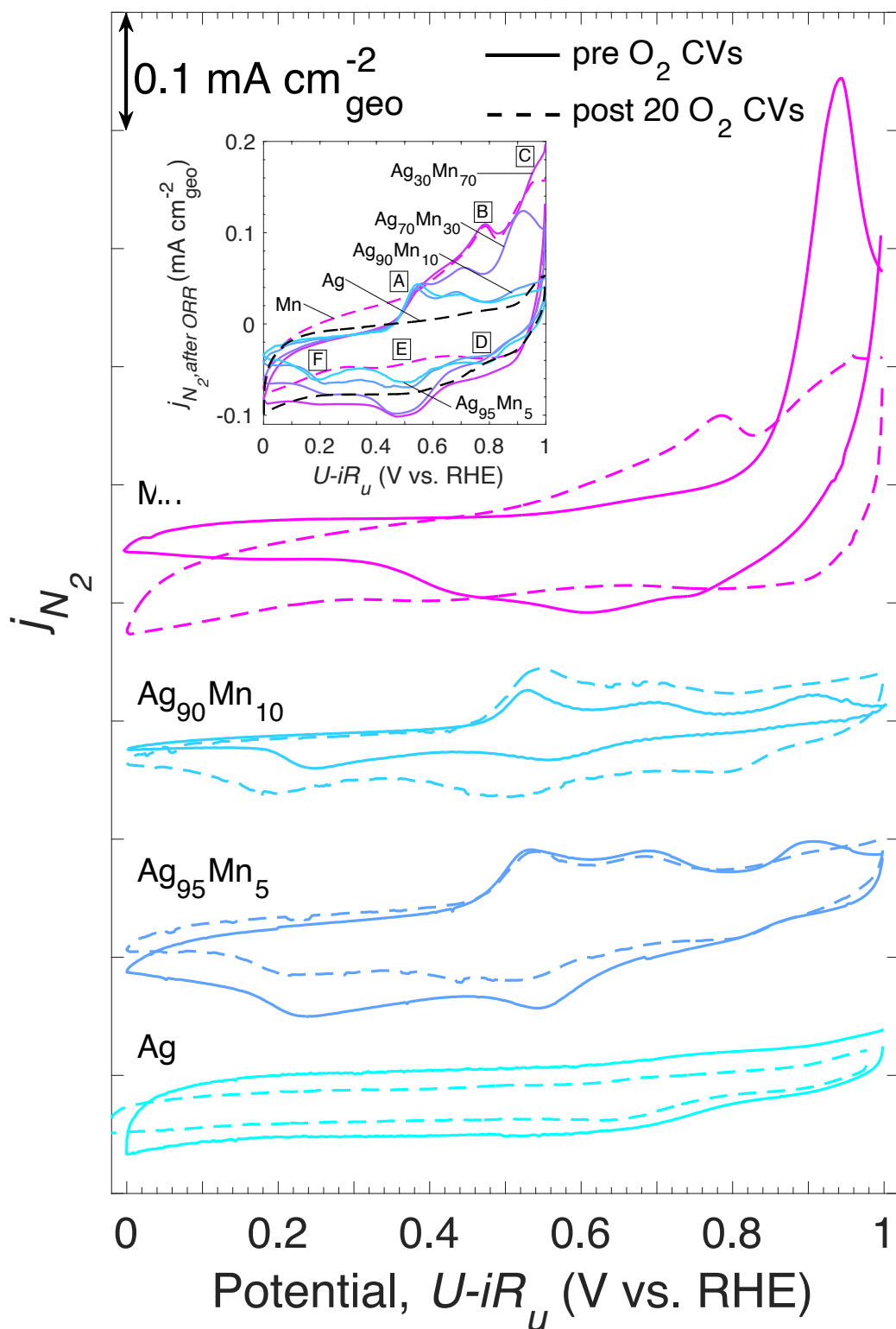


Figure S14. Representative select characteristic CVs (2nd cycle), before (solid lines, -) and after (dashed lines, --) 20 O_2 CVs, of the $\text{Ag}_x\text{Mn}_{1-x}$ thin films. Minor absolute current density changes in the before and after curves, for example of Ag, are likely due to minor differences in trace dissolved O_2 . The inset corresponds to the overlaid representative characteristic CVs of the $\text{Ag}_x\text{Mn}_{1-x}$ thin films, measured post-ORR, with the noticeable redox peaks labeled from A-F for reference (Ag and Mn are shown with dashed lines for visual purposes).

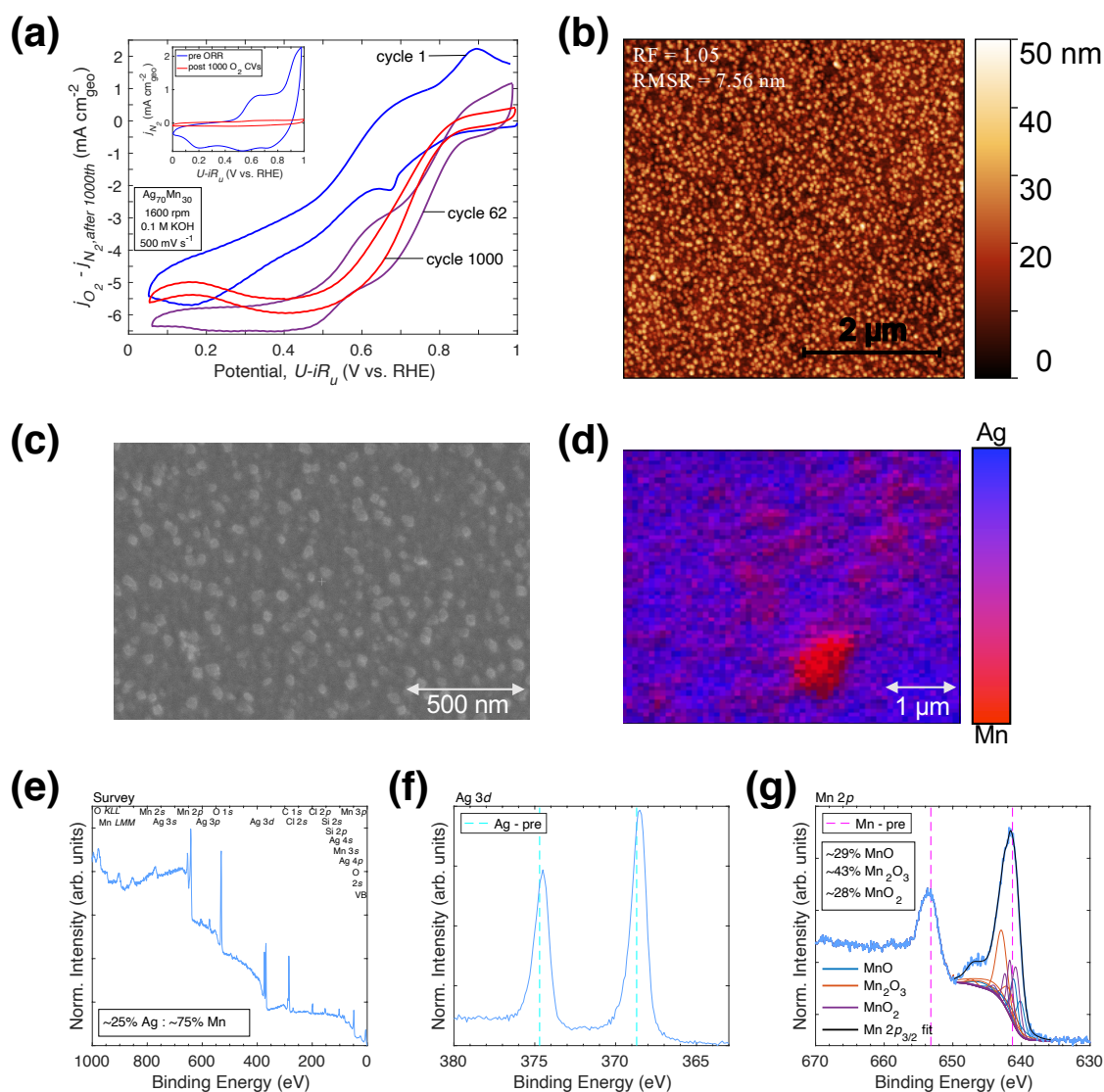


Figure S15. Representative stability testing and post-test physical characterization of $\text{Ag}_{70}\text{Mn}_{30}$. **(a)** Representative CVs (cycle 1: blue, cycle 62: purple, cycle 1000: red) of an electrocatalytic stability test of over 1000 cycles from 1 – 0 V vs. RHE at 500 mV s^{-1} , with an inset of the N_2 CV before and after testing. The average (cathodic/anodic) onset potential (defined at $-0.1 \text{ mA cm}_{\text{geo}}^{-2}$) increases from 0.81 V for cycle 1 to 0.9 V for cycle 62 and then decreases to 0.89 V vs. RHE for cycle 1000. The average (cathodic/anodic) kinetic current density (j_k) at 0.8 V vs. RHE changes from $0.1 \text{ mA cm}_{\text{geo}}^{-2}$ for cycle 1 to $-1.7 \text{ mA cm}_{\text{geo}}^{-2}$ for cycle 62 and then to $-0.7 \text{ mA cm}_{\text{geo}}^{-2}$ for cycle 1000 (the $j_{k,0.8V}$ for the cathodic, and most active, sweep changes from -0.7 to -2.2 to $-0.9 \text{ mA cm}_{\text{geo}}^{-2}$). **(b)** AFM topography ($5 \mu\text{m} \times 5 \mu\text{m}$) post stability measurements ($\text{RF} = 1.054$ and RMS Roughness (RMSR) = 7.559 nm). **(c)** SEM imaging (secondary electron detector) and **(d)** overlaid Ag/Mn AES elemental map post stability testing at a large nano-island-like feature (separate from SEM in (c)). Within AES resolution (tens of nanometers), Ag and Mn remain mixed after stability measurements (also see Figure S16e–h), although there appears to be some local surface Mn-phase segregation. **(d)** Survey XPS, **(e)** Ag $3d$ HR XPS, **(f)** Mn $2p$ HR XPS of the $\text{Ag}_{70}\text{Mn}_{30}$ thin film map post stability testing. In (d), Cl likely comes from general contamination in air and/or the Ag/AgCl reference electrode, and the Si likely comes from general contamination in air and/or from glass corrosion due to operating glassware at pH 13 for extended periods of time (which is one of the downsides of stability testing in RDE).

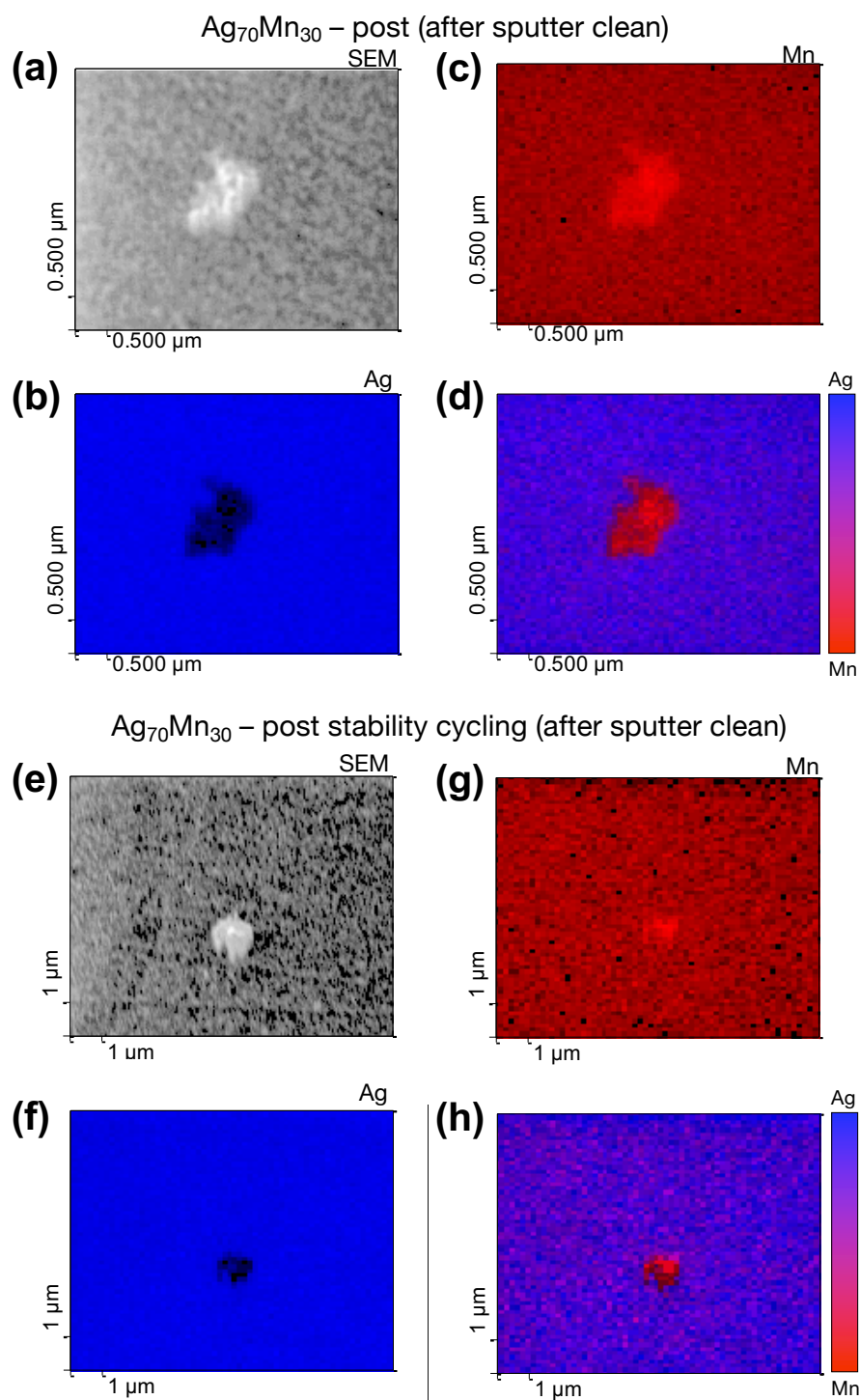


Figure S16. Representative AES showing an SEM (secondary electron detector) image with corresponding Ag, Mn, and overlaid Ag/Mn AES elemental mapping of selected areas with potential nano-island-like features on $\text{Ag}_{70}\text{Mn}_{30}$ after ORR testing (**a–d**) and after ORR stability testing (**e–h**; see also Figure S15). In **a–d**, post stability cycling is 20 CVs in O_2 + 2 CVs in N_2 , 20 mV s^{-1} at 1600 rpm, and in **e–h**, post ORR is 1000 CVs in O_2 + 2 CVs in N_2 , 500 mV s^{-1} at 1600 rpm. These samples were cleaned with Ar^+ sputtering after visually locating desired features on the SEM imaging monitor.

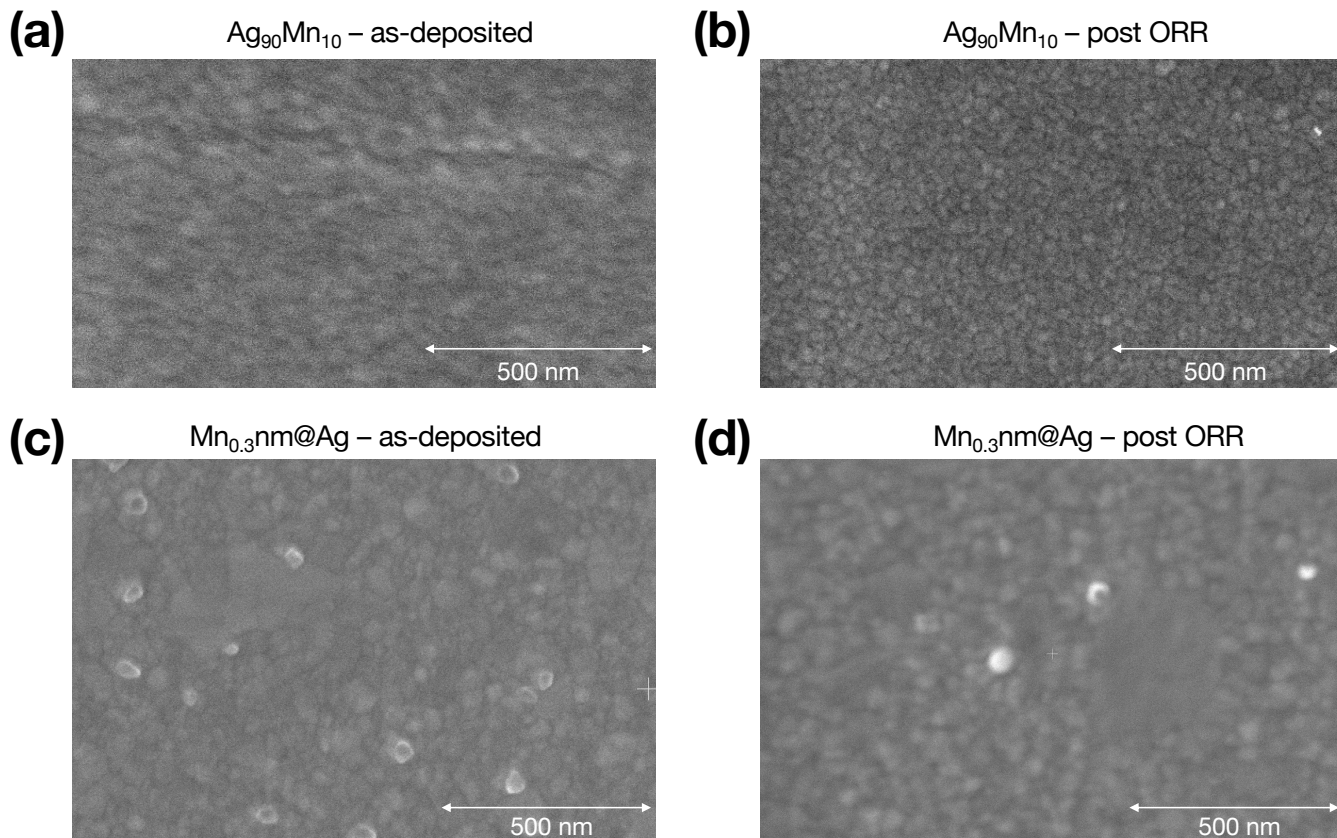


Figure S17. Representative SEM imaging in standard mode with an Everhart Thornley Detector (ETD) of **(a-b)** $\text{Ag}_{90}\text{Mn}_{10}$ and **(c-d)** $\text{Mn}_{0.3\text{nm}}\text{@Ag}_{69.7\text{nm}}$ before (as-deposited) and after (post) ORR testing. Electron beam settings: 5 kV and 50 pA. The bright white circular features in **(c-d)** are hypothesized to be thin MnO_x nano-islands as suggested by AES mapping (**Supplementary Figures S20–S22**), although this cannot be confirmed from this SEM images alone. These images **(c-d)** alone only indicate that these features are taller and/or of different average composition than the underlying surrounding area.

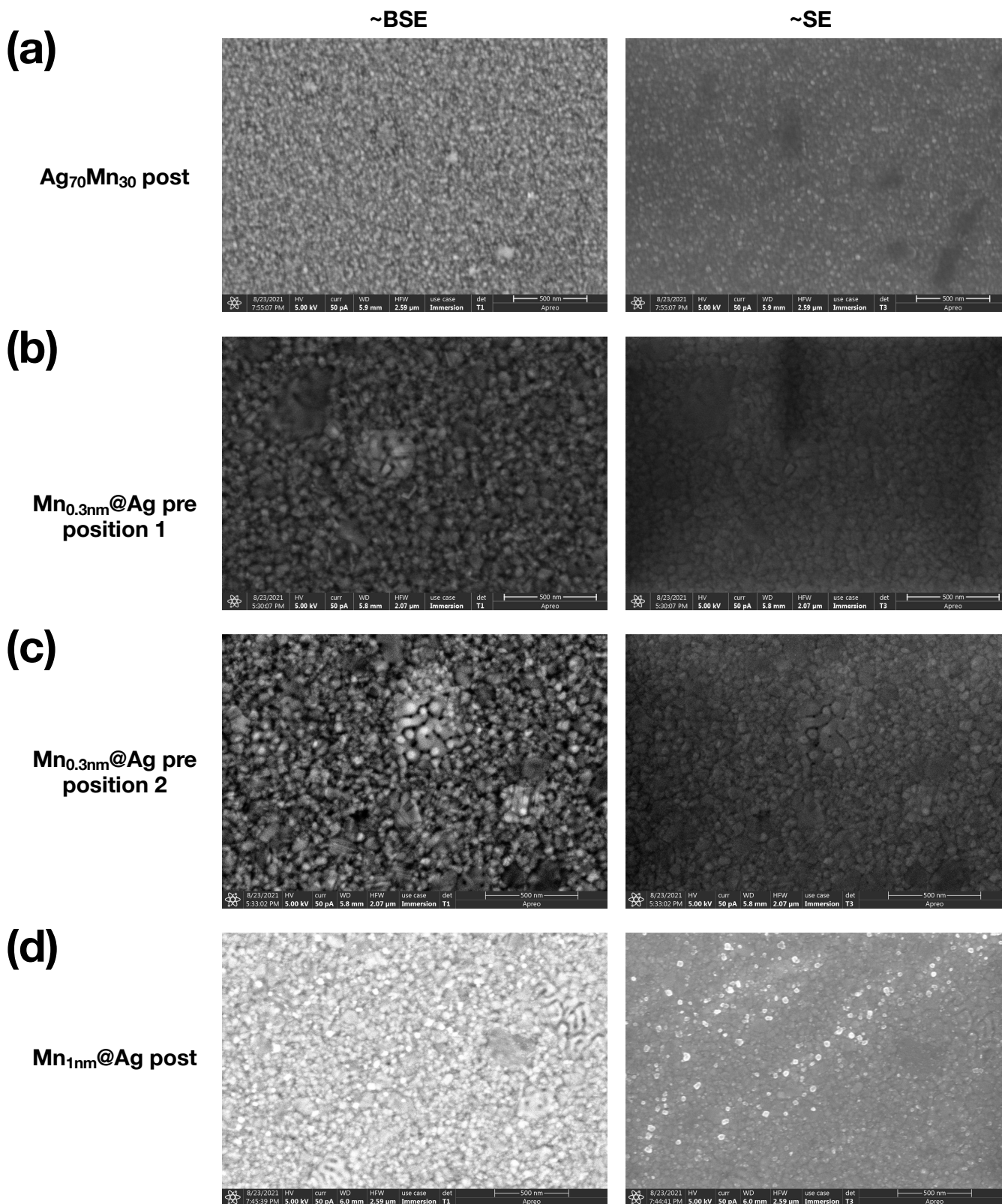


Figure S18. Representative SEM imaging of **(a)** $\text{Ag}_{70}\text{Mn}_{30}$ post-ORR testing, **(b-c)** $\text{Mn}_{0.3\text{nm}}\text{@Ag}$ before (as-deposited) and **(d)** after (post-)ORR testing. The left column shows the images collecting almost exclusively backscattered electrons (~BSE) and the right column the images collecting almost exclusively secondary electrons (~SE). Electron beam settings: 5 kV and 50 pA.

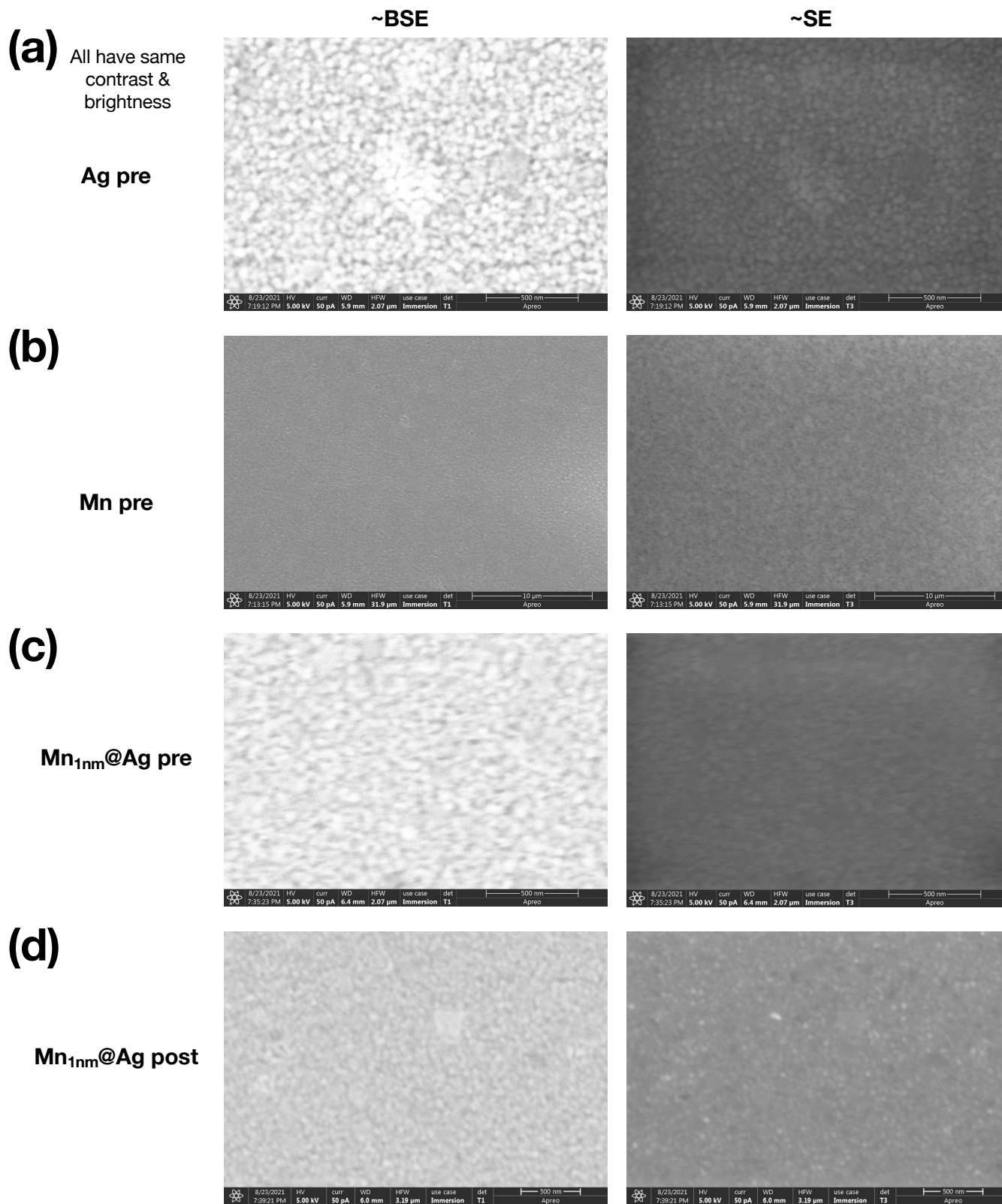


Figure S19. Representative SEM imaging, with the same contrast & brightness, of as-deposited (pre-ORR) (a) Ag, (b) Mn, and of Mn_{1nm}@Ag (c) pre (as-deposited) and (d) post-ORR testing. The left column shows the images collecting almost exclusively backscattered electrons (~BSE) and the right column the images collecting almost exclusively secondary electrons (~SE). Electron beam settings: 5 kV and 50 pA.

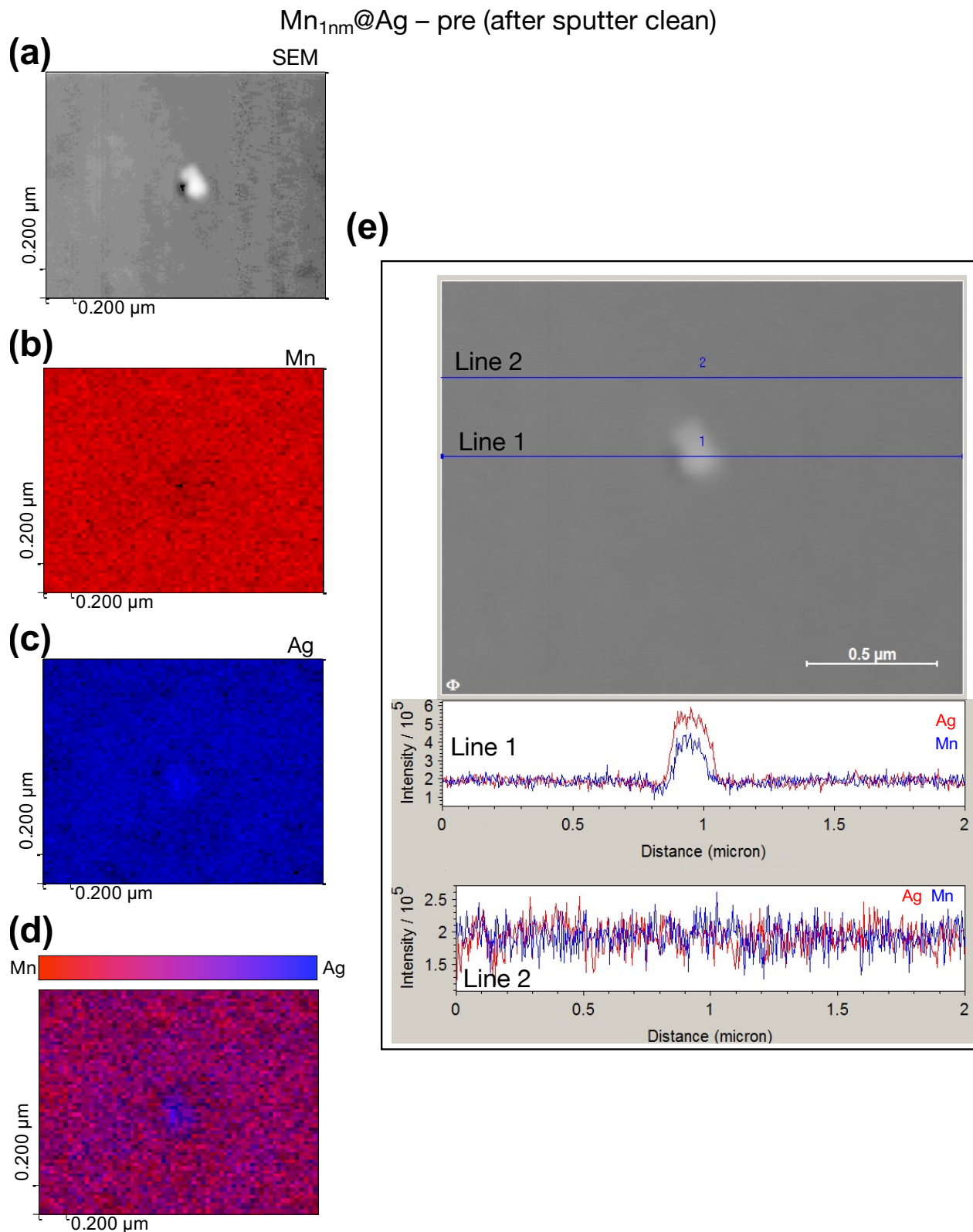


Figure S20. Representative AES showing an SEM (secondary electron detector) image with corresponding Ag, Mn, and overlaid Ag/Mn AES elemental mapping, (a–d) respectively, of a selected area with a potential nano-island-like feature on as-deposited $\text{Mn}_{1\text{nm}}@\text{Ag}$, and (e) corresponding Ag/Mn line scans of the feature and the surrounding area. This sample was cleaned with Ar^+ sputtering after visually locating the desired feature on the SEM monitor. Note the color ID (red/blue) changes between the line and 2D maps.

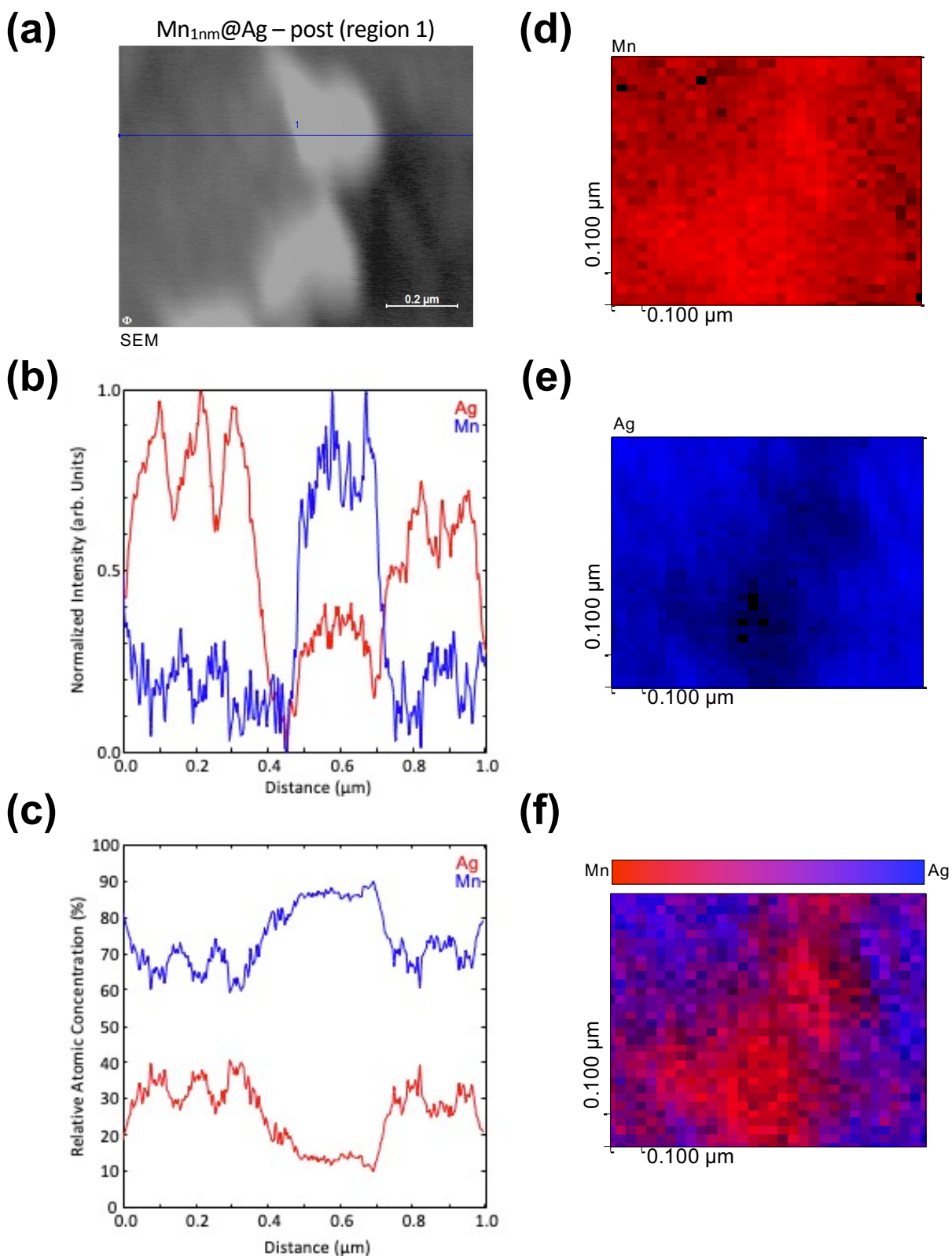


Figure S21. Representative AES showing an (a) SEM image (secondary electron detector) of a selected area (region 1) with a potential nano-island-like feature on post-ORR testing Mn_{1nm}@Ag, (b,c) corresponding Ag/Mn line scan of the feature showing normalized intensity and relative estimated atomic concentration respectively, and corresponding (d-f) Ag, Mn, and overlaid Ag/Mn AES elemental mapping, respectively. Post ORR is 20 CVs in O₂ + 2 CVs in N₂, 20 mV s⁻¹ at 1600 rpm. Note the color ID (red/blue) changes between the line and 2D maps.

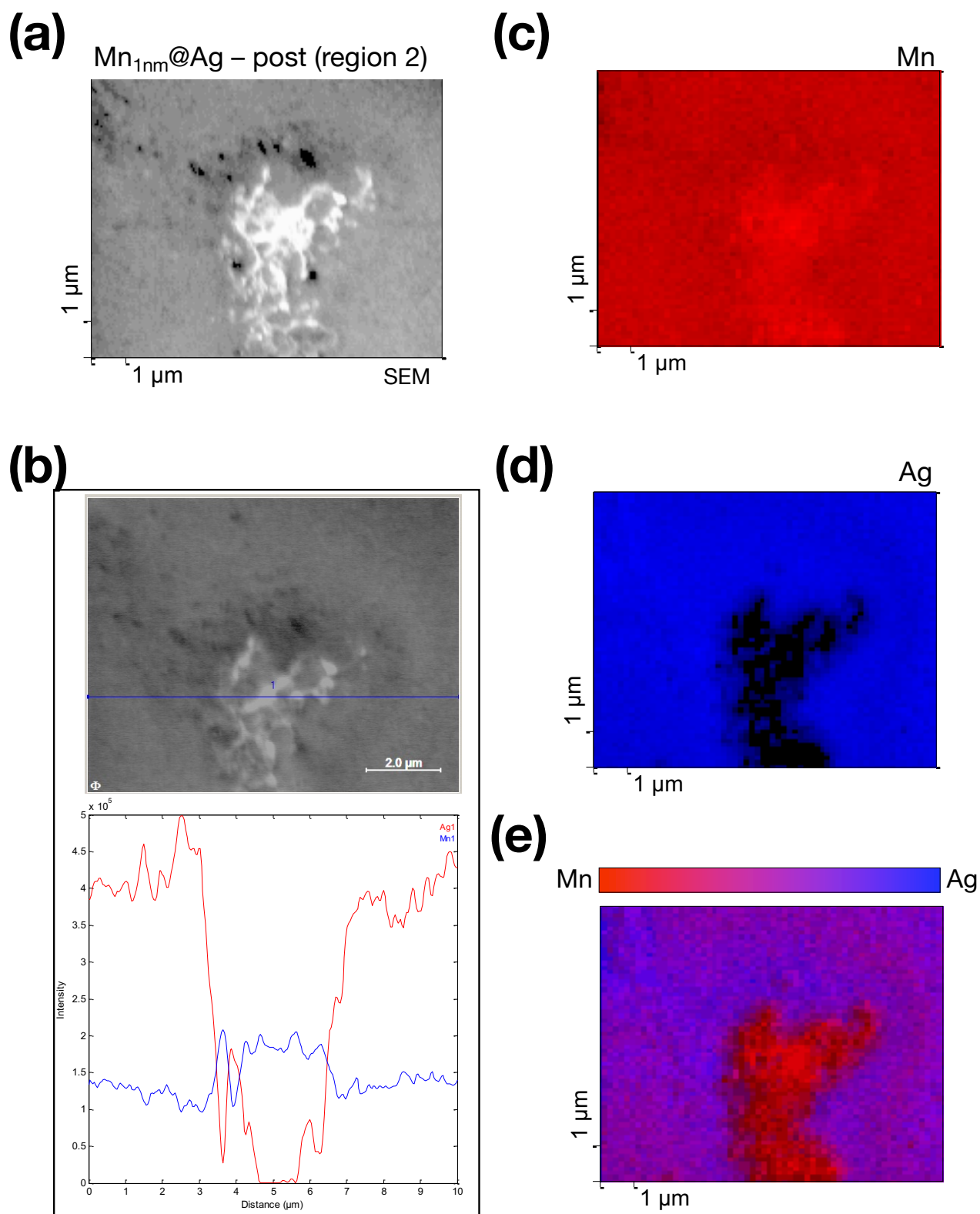


Figure S22. Representative AES showing an (a) SEM image (secondary electron detector) of a selected area (region 2) with a potential nano-island-like feature on post-ORR testing Mn_{1nm}@Ag, (b) corresponding Ag/Mn line scan of the feature showing normalized intensity, and corresponding (c–e) Ag, Mn, and overlaid Ag/Mn AES elemental mapping, respectively. Post ORR is 20 CVs in O₂ + 2 CVs in N₂, 20 mV s⁻¹ at 1600 rpm. Note the color ID (red/blue) changes between the line and 2D maps.

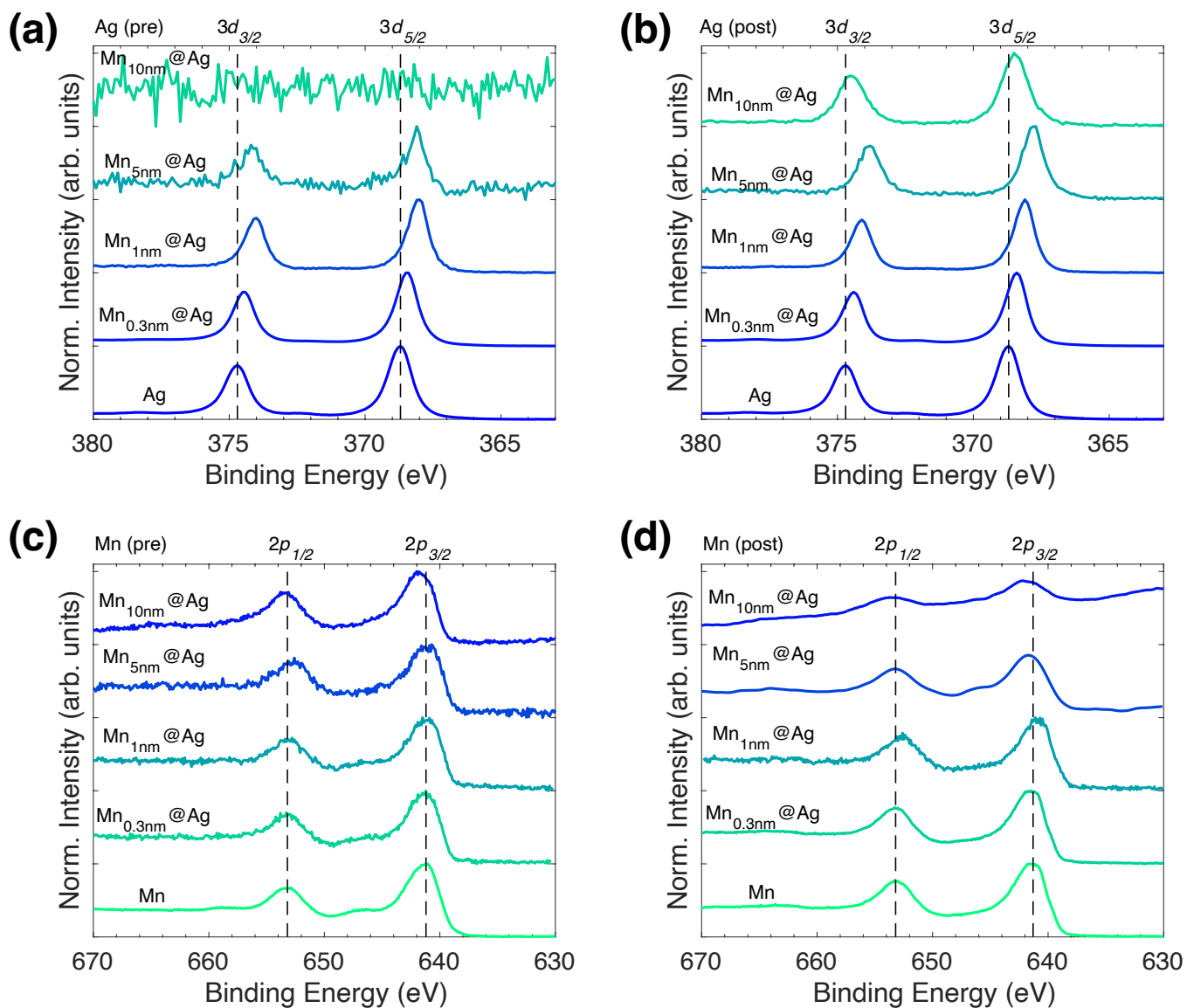


Figure S23. HR (a,b) Ag 3d and (c,d) Mn 2p XPS spectra of Mn_n@Ag before (a,c) and after (b,d) ORR testing.

Table S7. Ag/Mn quantification (representative from Su and HR XPS) and Mn-oxide species compositional analysis from fitted HR XPS Mn $2p_{3/2}$ spectra of $Mn_y@Ag$ before and after ORR testing. See graphical representative fitting procedure in **Supplementary Figure S4**. The average valency is average based on the oxidation state composition of the Mn $2p_{3/2}$ fit in this table: Avg. Mn Valency = $2 \cdot (Mn^{2+}\%) + 2.835 \cdot (Mn^{2.835+}\%) + 4 \cdot (Mn^{4+}\%)$. The trends in XPS composition and oxidation/valency are reliable; however, the absolute values have a possible intrinsic technique error of at least ~ 10 at%.¹ It is standard for XPS metal peaks (i.e. Ag) to be analyzed via Tougaard background correction, while XPS peaks for oxides (i.e. $Mn^{>0+}$) are generally analyzed with a Shirley background correction.¹ However, for the purposes of comparison between relative Ag-Mn elemental compositions a Tougaard background correction was employed. Because this is not ideal for Mn there is some added systematic error in the absolute values of Ag:Mn composition.¹ Considering the intrinsic technique/analysis error, plus select duplicate or triplicate measurements (on both the same and/or separate samples) of some Ag_xMn_{1-x} thin films, we observe errors from ± 5 -20 at% for Ag, Mn, and Mn-oxide fit compositions. For Mn $2p_{3/2}$ peak fitting, a Shirley background correction was employed.

	pre							post						
	Quant.		HR Mn $2p_{3/2}$ Fit					Avg. Mn Valency	Quant.		HR Mn $2p_{3/2}$ Fit			
	Ag	Mn	MnO (Mn ²⁺) (at%)	Mn ₂ O ₃ (Mn ³⁺) + Mn ₃ O ₄ (Mn ^{2.67+}) (Mn ^{2.835+}) (at%)	MnO ₂ (Mn ⁴⁺) (at%)		Mn 3s Splitting (eV)		Ag	Mn	MnO (Mn ²⁺) (at%)	Mn ₂ O ₃ (Mn ³⁺) + Mn ₃ O ₄ (Mn ^{2.67+}) (Mn ^{2.835+}) (at%)	MnO ₂ (Mn ⁴⁺) (at%)	Avg. Mn Valency
Ag	100	0	N/A	N/A	N/A	N/A	N/A	100	0	N/A	N/A	N/A	N/A	N/A
Mn_{0.3nm}@Ag	87	13	45	44	11	2.6	No signal	98	2	22	38	40	3.1	No signal
Mn_{1nm}@Ag	56	44	53	30	17	2.6	5.6	84	16	30	48	21	2.8	No signal
Mn_{5nm}@Ag	2	98	60	17	22	2.6	5.9	12	88	41	12	47	3.0	5.4
Mn_{10nm}@Ag	0	100	51	11	38	2.8	5.9	2	98	30	51	19	2.8	5.4
Mn	0	100	75	22	3	2.2	5.9	0	100	34	31	35	3.0	5.6

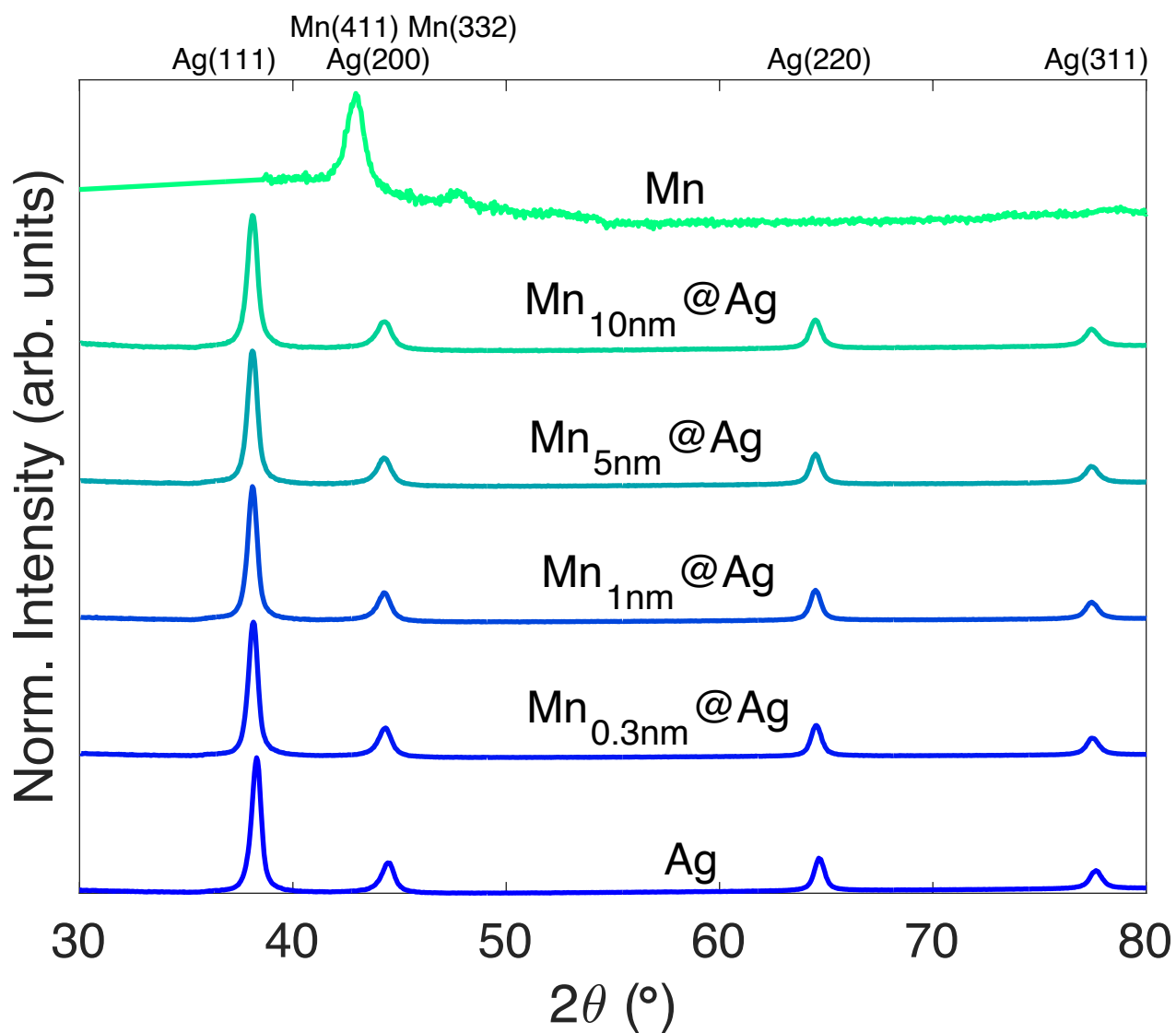


Figure S24. GI XRD of as-deposited Mn_n@Ag (on standard glass slides to increase are of x-ray illumination and avoid background interferences from glassy carbon).

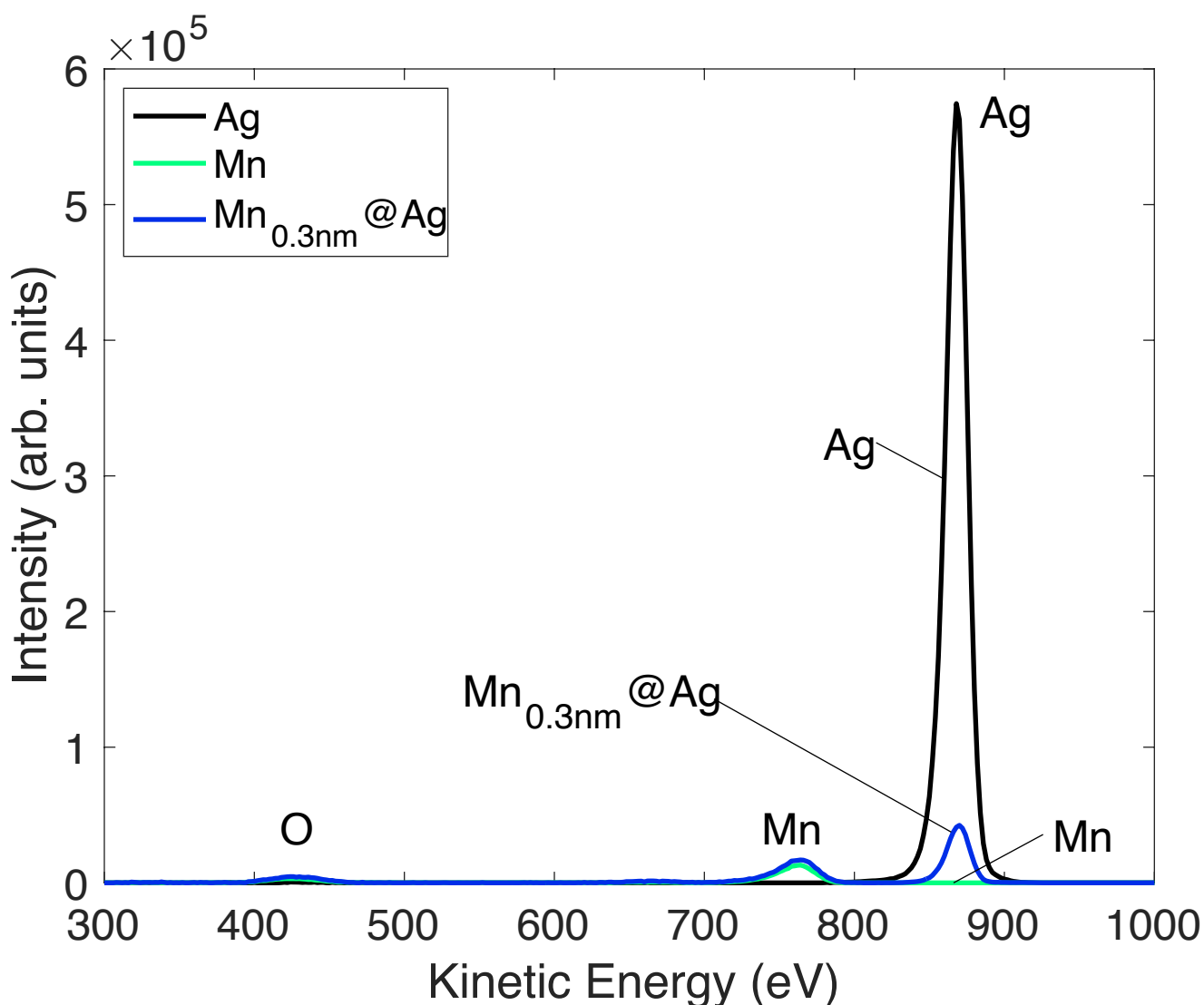


Figure S25. Representative He low energy ion scattering (LEIS) spectra for as-deposited (air-exposed) Ag, Mn, and $\text{Mn}_{0.3\text{nm}}@Ag$ thin films deposited on a Si(111) substrate. Line-text-labels correspond to the data curves and plain text labels to the element peak. These data were collected by Thermo Fisher as a complimentary (and limited) technique demonstration (not all experimental/measurement parameters/settings were disclosed to us). The LEIS spectra shown here is baseline-subtracted (done in OriginPro). In agreement with the XPS spectra shown in this work, the XPS (not shown here for brevity) of the samples used for LEIS indicate that Mn is in a dominant Mn^{2+} valency and that Ag is metallic (see representative XPS for the samples in **Supplementary Figure S23 and Tables S5,S11**). As a top-most layer sensitive technique,¹⁰ the LEIS shown here demonstrates, that indeed, as hypothesized based on CV and XPS measurements discussed in this work, the $\text{Mn}_{0.3\text{nm}}@Ag$ sample is not fully coated by Mn despite 0.3 nm being the theoretical thickness equivalent of a Mn metal monolayer. For $\text{Mn}_{0.3\text{nm}}@Ag$, the Ag:Mn:O peak area ratio is 52:36:12 and the Ag:Mn area ratio is 59:41. Comparing the $\text{Mn}_{0.3\text{nm}}@Ag$ sample to the standard Ag and Mn thin film samples, the Mn and O peaks are similar between $\text{Mn}_{0.3\text{nm}}@Ag$ and Mn, while the Ag peak area for $\text{Mn}_{0.3\text{nm}}@Ag$ is $\sim 10\%$ of the pure Ag metal peak area. Quantitative compositional analysis is difficult without knowing the exact scattering cross sections of each element.

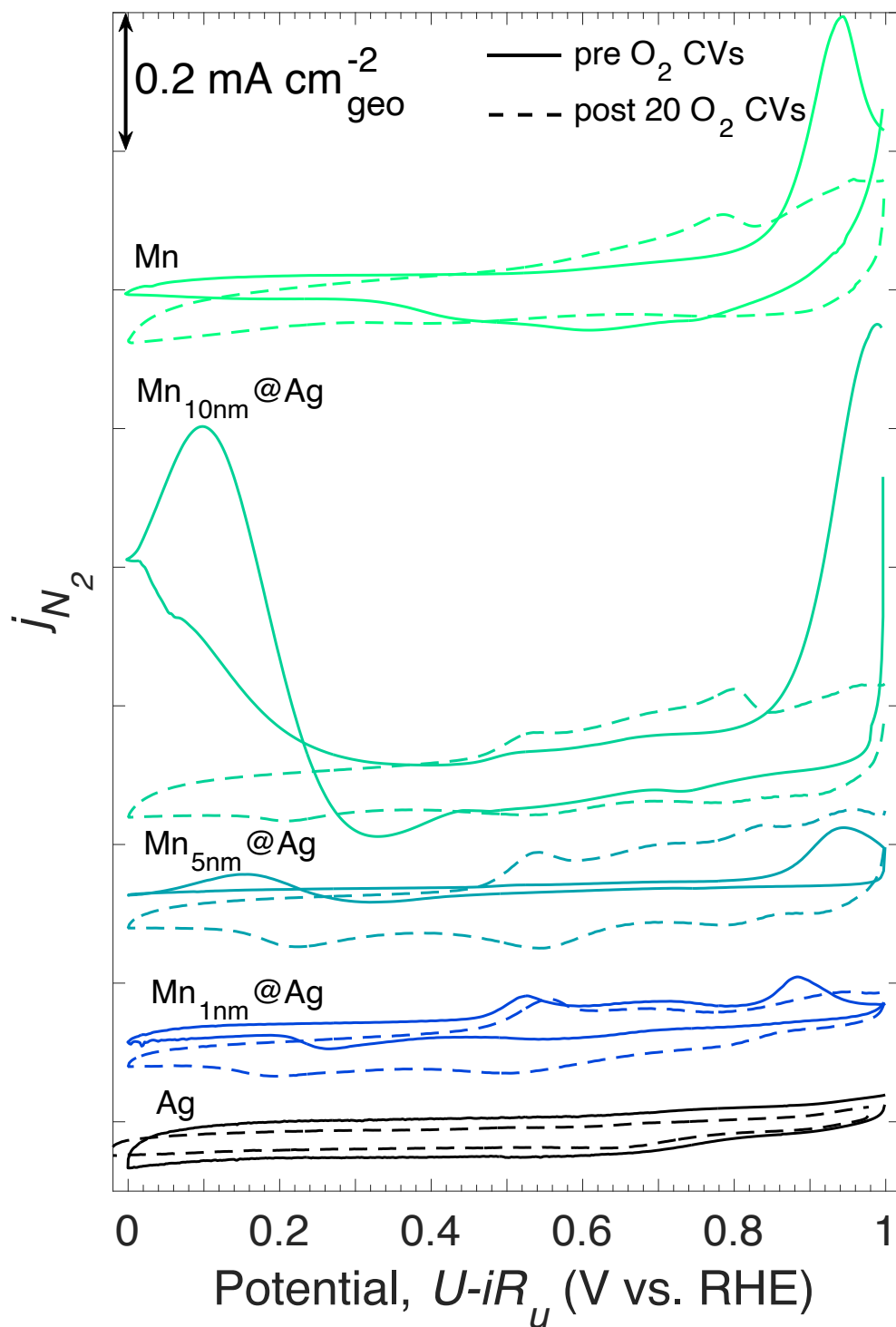


Figure S26. Representative select characteristic CVs (2nd cycle), before (solid lines) and after (dashed lines) 20 O_2 CVs, of the $\text{Mn}_y @ \text{Ag}$ thin films. The $y = 5$ and 10 nm films exhibit an unusual, positive current, feature on the cathodic/reductive sweep from around 0.3 to 0 V vs. RHE, that has been observed previously¹¹ on Mn thin films and attributed to irreversible changes likely with respect to the surface oxidation state/surface structure and/or Mn dissolution. Minor absolute current density changes in the before and after curves, for example of Ag, are likely due to minor differences in trace dissolved O_2 .

Table S8. Summary of physically representative ORR mass activities (MA_s) for the first, ~best, and final (20th) cycle for Ag_xMn_{1-x} and $Mn_y@Ag$. Average (AVG) and standard deviation (STDEV) from at least triplicate measurements (with separate samples and electrolyte). MA_s were calculated by dividing the specific activity at 0.8 V_{RHE} (**Supplementary Table S6**) by the Ag or Mn mass loading as defined/stated in the table headers. For the Ag-normalized mass activities, we divide by $\sim 0.315 \mu g cm_{geo}^{-2}$, which corresponds to approximately one monolayer (ML) coverage of Ag (~ 0.3 nm thickness) and is the upper limit on the possible Ag mass loading at the active surface (naturally, this mass loading overestimates the amount of Ag at the surface of the Ag_xMn_{1-x} and $Mn_y@Ag$ thin films, which would be difficult to accurately and precisely calculate; i.e. note that according to XPS, there is little to no Ag in the near-surface of $Ag_{30}Mn_{70}$, $Mn_{5nm}@Ag$, and $Mn_{10nm}@Ag$). Moreover, in the initial stages of this work, we observed 40 nm thin films of Ag_xMn_{1-x} ($x = 0, 30, 70, 100$) perform the same as the 70 nm films reported in this work, indicating that indeed intrinsic ORR activity is independent of film thickness in the order of tens of nanometers (this is consistent with previous work^{3, 12} on Ag-Cu thin films which showed consistent performance across various thicknesses). Owing to the more dynamic nature of Mn, namely its oxidation, migration toward the surface, and possible phase-segregation upon air exposure, it is difficult to propose the most appropriate Mn mass loading values for activity normalization. Therefore, we employ the total deposited Mn (metal) mass loading deposited by PVD. We note this is most accurate for the $Mn_y@Ag$ system in which there is no bulk MnO_x/Mn by design. Note that these metrics do not necessarily account for the complete overall CV performance for $Ag_{30}Mn_{70}$, $Mn_{5nm}@Ag$, and $Mn_{10nm}@Ag$, which overall perform worse than Ag (**Supplementary Fig. S13**).

cycle	sample	Total PVDed Mn mass loading ($mg cm_{geo}^{-2}$)	Normalization by Ag ML (0.3 nm of Ag = $\sim 3.1E-04 mg cm_{geo}^{-2}$)		Normalization by total Mn	
			AVG $MA_{k,Ag}$ at 0.8 V_{RHE} ($mA mg_{Ag}^{-1} ML$)	STDEV $MA_{k,Ag}$ at 0.8 V_{RHE} ($mA mg_{Ag}^{-1} ML$)	AVG $MA_{k,Mn}$ at 0.8 V_{RHE} ($mA mg_{Mn}^{-1}$)	STDEV $MA_{k,Mn}$ at 0.8 V_{RHE} ($mA mg_{Mn}^{-1}$)
20	Mn	5.0E-02	-	-	-1.6E+00	5.4E-01
3	Ag	-	-8.7E+02	2.7E+02	-	-
1	$Ag_{30}Mn_{70}$	3.5E-02	-9.6E+02	2.2E+02	-8.6E+00	1.9E+00
	$Ag_{70}Mn_{30}$	1.5E-02	-1.7E+03	1.4E+03	-3.5E+01	2.9E+01
	$Ag_{90}Mn_{10}$	5.0E-03	-2.4E+03	1.2E+03	-1.5E+02	7.8E+01
	$Ag_{95}Mn_5$	2.5E-03	-2.2E+03	7.5E+02	-2.8E+02	9.4E+01
~best	$Ag_{30}Mn_{70}$	3.5E-02	-8.4E+02	3.7E+02	-7.5E+00	3.3E+00
	$Ag_{70}Mn_{30}$	1.5E-02	-4.7E+03	4.2E+02	-9.8E+01	8.8E+00
	$Ag_{90}Mn_{10}$	5.0E-03	-6.1E+03	1.7E+03	-3.8E+02	1.1E+02
	$Ag_{95}Mn_5$	2.5E-03	-8.5E+03	2.1E+03	-1.1E+03	2.6E+02
20	$Ag_{30}Mn_{70}$	3.5E-02	-3.7E+02	1.7E+02	-3.3E+00	1.5E+00
	$Ag_{70}Mn_{30}$	1.5E-02	-2.4E+03	3.3E+02	-5.0E+01	6.9E+00
	$Ag_{90}Mn_{10}$	5.0E-03	-2.4E+03	5.8E+02	-1.5E+02	3.6E+01
	$Ag_{95}Mn_5$	2.5E-03	-2.7E+03	8.8E+02	-3.3E+02	1.1E+02
1	$Mn_{0.3nm}@Ag$	2.2E-04	-1.7E+03	6.5E+02	-2.5E+03	9.5E+02
	$Mn_{1nm}@Ag$	7.2E-04	-2.9E+03	1.5E+03	-1.3E+03	6.5E+02
	$Mn_{5nm}@Ag$	3.6E-03	-1.2E+03	2.5E+02	-1.1E+02	2.2E+01
	$Mn_{10nm}@Ag$	7.2E-03	-1.6E+03	5.0E+02	-6.8E+01	2.2E+01
~best	$Mn_{0.3nm}@Ag$	2.2E-04	-7.2E+03	1.3E+03	-1.1E+04	1.9E+03
	$Mn_{1nm}@Ag$	7.2E-04	-5.8E+03	9.0E+02	-2.5E+03	4.0E+02
	$Mn_{5nm}@Ag$	3.6E-03	-2.5E+03	9.5E+02	-2.2E+02	8.3E+01
	$Mn_{10nm}@Ag$	7.2E-03	-1.6E+03	5.0E+02	-6.9E+01	2.2E+01
20	$Mn_{0.3nm}@Ag$	2.2E-04	-2.5E+03	1.0E+03	-3.6E+03	1.5E+03
	$Mn_{1nm}@Ag$	7.2E-04	-3.4E+03	6.5E+02	-1.5E+03	2.8E+02
	$Mn_{5nm}@Ag$	3.6E-03	-2.0E+03	7.9E+02	-1.8E+02	6.9E+01
	$Mn_{10nm}@Ag$	7.2E-03	-1.0E+03	3.0E+02	-4.4E+01	1.3E+01

Table S9. Representative literature summary of Ag-Mn ORR electrocatalyst performance in alkaline conditions with an RDE. Note that quantitative comparison to the performance of our $\text{Ag}_x\text{Mn}_{1-x}$ and $\text{Mn}_y@\text{Ag}$ thin films is difficult because the vast majority of the Ag-Mn ORR literature reports performance metric on a geometric (geo) electrode area basis, which is not representative of intrinsic (specific) activity in nanoparticulate/powder-ink electrocatalyst systems. A hyphen (-) indicates we could not find the information. The non-gray highlighted j_k entries correspond to the data as read (in text or graphically) from the literature, while the gray-highlighted entries correspond to the j_k calculated by us, with the Koutecký-Levich equation, from literature provided CVs. LCD is low current density.

Catalyst Material	$j_{k,0.8 V_{\text{RHE}}}$ (mA cm ⁻²) Reported or Calculated (gray)	Tafel Slope (mV dec ⁻¹) Reported at LCD	$MA_{k,0.8 V_{\text{RHE}}}$ Reported (mA _k mg _{cat} ⁻¹)	Scan Rate (mV s ⁻¹)	Electrolyte	Reported basis for kinetic current normalization	Ref
50wt% Ag-MnO ₂ /C	0.6	89	-	5	0.1 M KOH	geo	13
MnO ₂ /C	0.1	169	-	5	0.1 M KOH	geo	13
Ag/C	0.2	97	-	5	0.1 M KOH	geo	13
20wt% Pt/C	17.6	86	-	5	0.1 M KOH	geo	13
Ag/C	0.3	-	-	20	0.1 M KOH	geo	14
Ag/Mn ₃ O ₄ /C	15.5	-	-	20	0.1 M KOH	geo	14
Pt/C premetek	25.2	60	-	20	0.1 M KOH	geo	14
Ag/graphene	0.1	57	-	10	0.1 M KOH	geo	15
MnO _x /graphene	0.4	96	-	10	0.1 M KOH	geo	15
Ag-MnO _x /graphene	0.2	85	-	10	0.1 M KOH	geo	15
bulk Pt	0.6	55	-	10	0.1 M KOH	geo	15
Ag-manganese oxide nanofibers (Ag-OSM-2)	0.8	55.3	32.9	5	0.1 M KOH	possibly BET or geo	16
Ag-MnO _x /VC	2.8	-	125.0	5	0.1 M KOH	geo	17
MnO _x /VC	1.0	-	60.0	5	0.1 M KOH	geo	17
Pt/VC	1.7	-	136.0	5	0.1 M KOH	geo	17
Pd/VC	1.6	-	111.0	5	0.1 M KOH	geo	17
VC	0.0	-	2.8E-02	5	0.1 M KOH	geo	17
Ag/VC	0.1	-	7.6	5	0.1 M KOH	geo	17
Mn ₃ O ₄ -Ag/C	10.0	60	-	5	1 M NaOH	geo	18
Ag/C	2.2	60	-	5	1 M NaOH	geo	18
Ag-MnO _x /C-fresh	0.1	-	-	100	0.1 M NaOH	geo	19
Ag-MnO _x /C-200	0.6	-	-	100	0.1 M NaOH	geo	19
Ag-MnO _x /C-300	1.1	-	-	100	0.1 M NaOH	geo	19
Ag-MnO _x /C-400	0.8	-	-	100	0.1 M NaOH	geo	19
Pt/C	3.6	-	-	100	0.1 M NaOH	geo	19
Ag-MnO _x /CNT	0.8	70	-	-	0.1 M KOH	estimated active area	20
Ag/CNT	1.2	70	-	-	0.1 M KOH	estimated active area	20
Ag-MnO _x /C-1	0.6	55	-	10	0.1 M NaOH	geo	21
Ag-MnO _x /C-2	0.9	55	-	10	0.1 M NaOH	geo	21
Ag/C	0.1	60	-	10	0.1 M NaOH	geo	21

α -MnO ₂	0.2	81	-	5	0.1 M KOH	geo	22
Ag-MnO ₂	0.5	77	-	5	0.1 M KOH	geo	22
Ag/C	0.1	80	-	5	0.1 M KOH	geo	22
30wt% Pt/C	3.7	52	-	5	0.1 M KOH	geo	22

Table S10. Mn_{atom}-Ag active site models investigated by DFT for their effect on ORR activity. Though it is extremely unlikely to have metallic Mn on the surface under ORR conditions, we were interested in evaluating the activity of a Ag(111) surface with a trapped single Mn atom (Mn_{atom}-Ag) representing a highly Ag-rich surface structure. Considering the Mn-Ag bridge site as the active site, the calculated limiting potential of Mn_{atom}-Ag is -0.32 V vs. RHE. Increasing the O* coverage at the vicinity of Mn_{atom} in Mn_{atom}-Ag site from 1O* and 2O*, increased the limiting potential to -0.26 V and -0.18 V, respectively. Therefore, these active sites do not correspond to the experimentally observed activity enhancement.

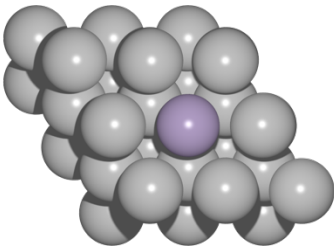
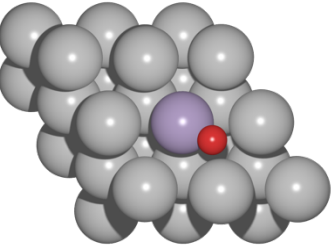
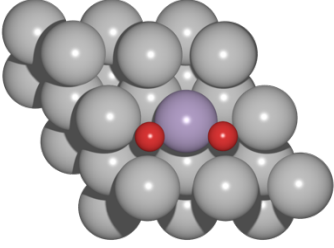
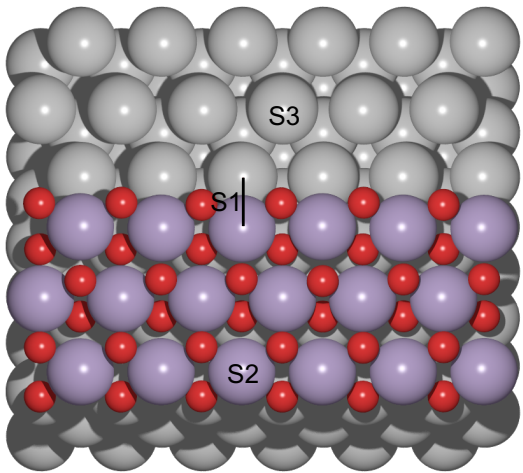
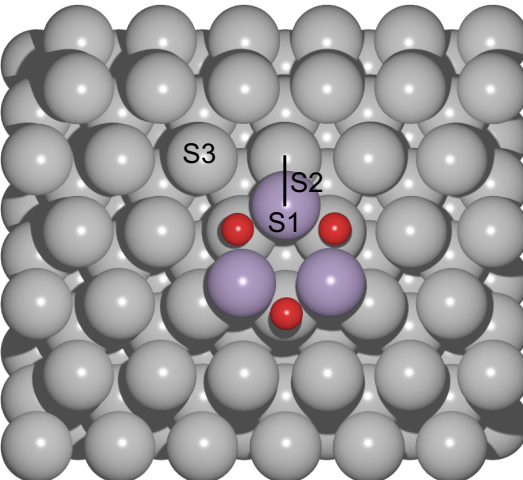
	Structure	U_L (V vs. CHE)
Mn _{atom} -Ag(111)		-0.32
1O*+ Mn _{atom} -Ag(111)		-0.26
2O*+ Mn _{atom} -Ag(111)		-0.18

Table S11. $\text{Mn}_{18}\text{O}_{36}$ nano-stripe@Ag(111) and MnO_x nano-island@Ag(111) models investigated by DFT for their effect on ORR activity. The formation energies are calculated using, $E_{\text{form}} = [n\text{MnO}_x@Ag(111) - Ag(111) - n\text{MnO}_2 + \mu_{\text{O}}]/n$ where $\text{MnO}_x@Ag(111)$, $Ag(111)$, and MnO_2 are the VASP calculated electronic energies of the total system, metallic Ag surface, and bulk Mn-oxide (pyrolusite MnO_2), n is the number of Mn atoms in the nano-scale structure, and μ_{O} is the chemical potential of the O calculated as the difference between gas phase H_2O and H_2 molecules. Multilayer MnO_x nano-structures on Ag(111) were not computationally stable.

Surface	Structure	Formation energy (eV per Mn atom)	U_L (V vs. CHE)
$\text{Mn}_{18}\text{O}_{36}$ nano-stripe@Ag(111)		-0.08	S1: 0.75 (Ag-Mn interface) S2: 0.42 (Mn top) S3: 0.39 (Ag top)
Mn_3O_3 nano-island@Ag(111)		-0.52	S1: 0.24 (Mn top) S2: 0.01 (Ag-Mn interface) S3: 0.61 (Ag top)

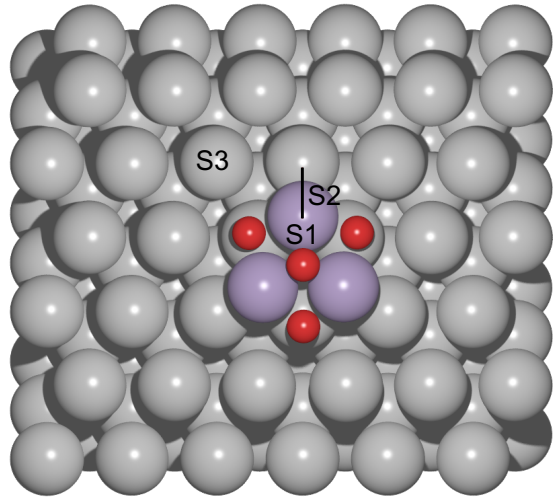
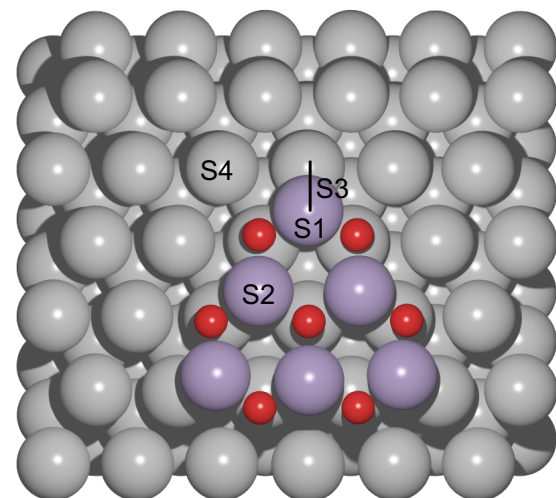
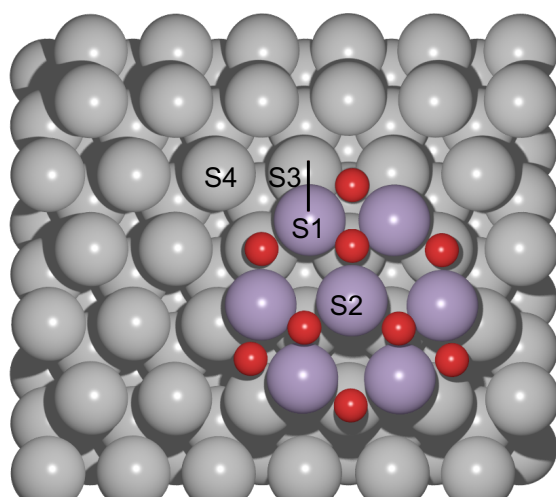
Mn ₃ O ₄ nano-island@Ag(111)		-0.03	S1: -0.01 (Mn top) S2: -0.06 (Ag-Mn interface) S3: 0.55 (Ag top)
Mn ₆ O ₇ nano-island@Ag(111)		-0.67	S1: 0.14 (Mn top) S2: 0.07 (Mn top) S3: 0.79 (Ag-Mn interface) S4: 0.48 (Ag top)
Mn ₇ O ₉ nano-island@Ag(111)		-0.75	S1: 0.73 (Mn top) S2: 0.63 (Mn top) S3: 0.81 (Ag-Mn interface) S4: 0.45 (Ag top)

Table S12. Evaluation of coverage effects on Mn₁₈O₃₆ nano-stripe@Ag(111).

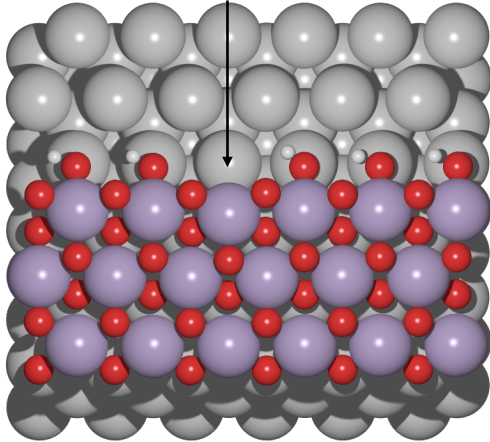
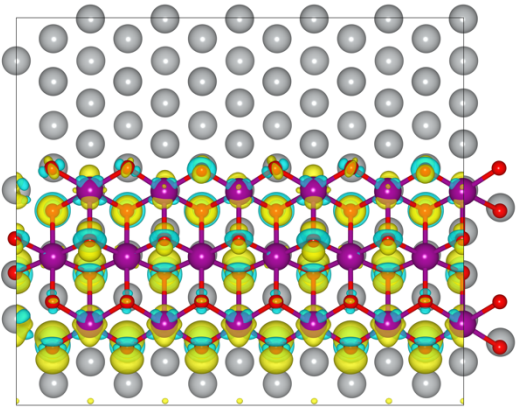
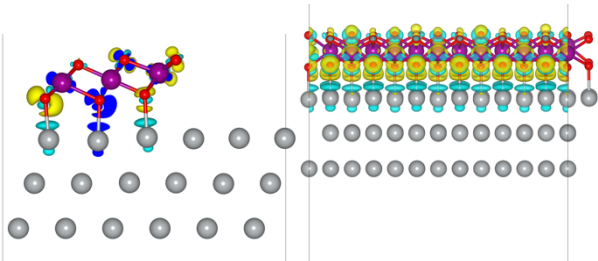
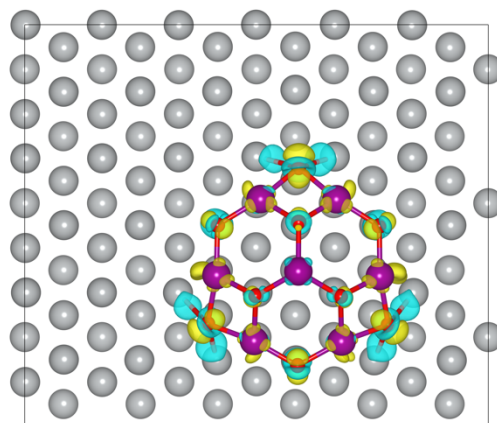
Surface	Structure	U_L (V vs. CHE)
Mn ₁₈ O ₃₆ nano-stripe@Ag(111)	 <p>Ag-Mn active site</p>	0.72

Table S13. The charge density difference plots indicating regions with depleted electron density in teal and excess electron density in yellow colors. Isosurface levels plotted from -0.0004 to $+0.0004$ e bohr⁻³.

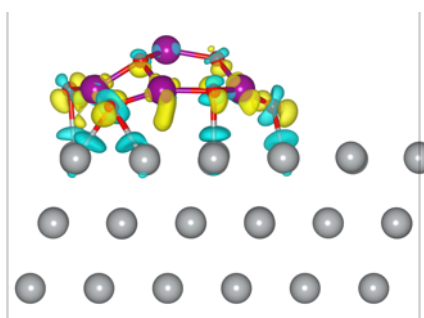
Surface	Charge density difference plots
Mn ₁₈ O ₃₆ nano-stripe@Ag(111)	<p>top-view</p>  <p>side-views</p> 

Mn₇O₉ nano-
island@Ag(111)

top-view



side-view



Supplementary Note S1: Results & discussion of comprehensive physical characterization of the as-deposited (air-exposed) $\text{Ag}_x\text{Mn}_{1-x}$ thin films

GI-XRD (**Fig. 2a**) of the $\text{Ag}_x\text{Mn}_{1-x}$ thin films was performed to probe the overall bulk crystal structure and Ag-Mn miscibility within the thin films. GI-XRD of the pure Ag film is indicative of a face-centered cubic (fcc) crystal structure, with a strong (111) peak at 38.2° .⁸ The diffractogram of the pure Mn film has two clear peaks, the (411) at 43.0° and the (332) at 47.8° , representative of the most intense peaks expected for an α -Mn metal body-centered cubic (bcc) phase (ICSD 42743, or Materials Project mp-35, **Supplementary Fig. S5**). For our mixed $\text{Ag}_x\text{Mn}_{1-x}$ films, with the exception of $\text{Ag}_{30}\text{Mn}_{70}$, for which the Mn (411) peak is overlapping with the Ag (200) peak, indicating an α -Mn phase, the diffractograms of all the other compositions are practically indistinguishable from that of pure Ag indicating that there is no measurable bulk Ag-Mn miscibility in any of the films. For Mn and $\text{Ag}_{30}\text{Mn}_{70}$, the absence of the lower intensity peaks associated with the bcc α -Mn structure (see reference pattern in **Supplementary Fig. S5**) in our measured diffractograms (**Fig. 2a**) suggests large peak broadening due to very small crystallites and/or a partial amorphous nature of the film. Moreover, we do not observe any diffraction peaks associated with the Mn-oxide phases,^{13, 14, 18, 20-23} which are expected; further below we describe efforts using x-ray spectroscopies (**Fig. 2b,c** and **Supplementary Figs. S1-S4,S10** and **Table S1,S5**) that reveal Mn-oxides make up the near-surface of our Mn film. The lack of oxide diffraction peaks could be due to the small fraction of the thin film volume that is occupied by MnO_x (top ~ 15 -30%),⁶ as evidenced by XPS depth profiling (**Fig. 2d** and **Supplementary Fig. S3**). This supports the hypothesis that bcc α -Mn metal is the dominant Mn crystal structure in the bulk of the Mn-containing films (as expected for Mn metal deposited by PVD)¹¹, and indicates that any crystalline MnO_x regions are composed of very small crystallites or not present in high enough concentrations to be detected⁶ by this bulk-technique. Overall, XRD of the $\text{Ag}_x\text{Mn}_{1-x}$ thin films indicates that Mn (metal and/or oxide) has a negligible effect on the bulk crystal structure of Ag and that there is no measurable bulk Ag-Mn miscibility.

While XRD does not indicate bulk Ag-Mn miscibility, other techniques reveal a high level of mixing. Specifically, XANES (**Figure 2b**, **Supplementary Fig. S9**), XPS (**Fig. 2c**, **Supplementary Figs. S1-S4,S10** and **Table S1,S5**), and Ag/Mn Auger electron spectroscopy of as the synthesized films (AES; **Fig. 2f**, **Supplementary Figures S6**), as well as representative post-ORR SEM-EDS elemental maps (**Supplementary Fig. S8**), indicate that the Ag and Mn are well-mixed with oxidized Mn on the surface. Well lateral dispersion of Ag and Mn in the near-surface can be seen in **Figure 2f** by the uniform color distribution from the AES map of a representative $\text{Ag}_{90}\text{Mn}_{10}$ film. This technique has near-surface sensitivity with lateral and depth resolution in the order of tens of nanometers. SEM-EDS is bulk sensitive and elemental maps of select representative $\text{Ag}_x\text{Mn}_{1-x}$ thin films post-ORR also show well Ag/Mn distribution throughout the 70 nm film top down and laterally. Interestingly, depth profile XPS (**Fig. 2d**) indicates that the near-surface region is $\sim 10 - 40$ % Mn-rich relative to the as-evaporated (in vacuum) nominal composition. This Mn surface enrichment is due to Mn migration towards the air/ O_2 -exposed surface and concomitant surface Mn oxidation is seen by XPS depth profiling (**Fig. 2d** and **Supplementary Figures S3**) and is predicted by DFT-segregation energies (**Supplementary Tables S2,S3**). Furthermore, high resolution (HR) XPS (**Supplementary Fig. S1** and **Table S1**) shows that the BE of the Ag $3d$ peaks shifts negatively by up to 0.5 eV when Ag is mixed with Mn, further suggesting good solid-solid mixing in accordance with the AES mapping (**Fig. 2f** and **Supplementary Fig. S6**).

Moreover, these negative BE shifts have been associated with upshifts in the Ag *d*-band center,^{8, 14} which could result in improved oxygen adsorption energies and have significant effects on catalytic activity.²⁴ HR Mn *2p* (**Supplementary Fig. S1**) XPS is more difficult to interpret because the peak and its relative changes in BE position can arise from core electronic interactions with Ag or from a different net oxidation state, for which the theoretical and fitted peak positions of the possible oxide species are within instrument resolution.^{2, 14} Total electron yield (TEY) Mn *L*_{3,2} XANES (*2p* → *3d* transition), however, gives insight into the influence of Ag-Mn mixing on the Mn *d*-band electronic structure in the top ~10 nm (**Fig. 2b**). Specifically, we see the normalized *L*_{3,2} area decreases (~15%) with increased Ag content between Ag₃₀Mn₇₀ and Ag₇₀Mn₃₀ (**Fig. 2b** and **Supplementary Fig. S9**), suggesting that there is a net shift in electron density from Ag to Mn, resulting in a decrease of Mn *3d*-holes.⁶

To further probe the surface oxidation states in the as-deposited Ag_{*x*}Mn_{1-*x*} thin films, we turned to deconvolution of the HR Mn XPS (**Supplementary Figs. S1,S3,S4** and **Supplementary Table S1**) and Mn *L*_{3,2} XANES. HR Mn *2p*_{3/2} peak fitting and Mn *3s* peak splitting analysis (**Supplementary Figs. S1,S3,S4** and **Supplementary Table S1**) indicates that while a variety of Mn oxide species are likely present in the as-synthesized thin films, MnO (Mn²⁺) is the dominant (> 50 %) species for all Ag-Mn combinations and pure Mn itself.² Furthermore, the shape of the Mn *L*_{3,2} XANES of the as-deposited films (**Figure 2b**) is consistent with that seen previously for MnO.⁶

Mn migration toward the surface, concomitant with Mn oxidation upon air exposure, as expected based on Ag-Mn segregation energies (**Supplementary Table S2,S3**) and as measured by XPS (discussed above), could lead to surface morphology changes and restructuring. Therefore, AFM (**Supplementary Fig. S8** and **Supplementary Table S4**) and representative SEM (**Supplementary Figs. S17,S18**) were performed on the as-deposited Ag_{*x*}Mn_{1-*x*} thin films to investigate surface topography and morphology. As expected for this PVD synthesis, AFM shows that all thin films have smooth surfaces, with roughness factors (RFs) ≤ 1.01 and root mean square roughnesses (RMSRs) ~2–5 nm, without significant topographical features (**Supplementary Table S4** and **Supplementary Fig. S8**). AFM, therefore, indicates that the geometric electrode area is approximately equal to the exposed catalyst surface area.^{7, 25, 26} Representative SEM imaging (**Supplementary Figs. S17,S18**), in agreement with AES mapping (**Fig. 2f** and **Supplementary Fig. S6**), of select as-deposited Ag_{*x*}Mn_{1-*x*} thin films further supports that the surfaces of the thin films lack significant morphological features.

Supplementary Note S2: Characteristic (baseline) CV of representative Ag_{*x*}Mn_{1-*x*} thin films in N₂-saturated electrolyte

To better understand the non-ORR current contributions and final state of the material *in situ*, CV under N₂-saturation was performed after ORR testing with the same Ag_{*x*}Mn_{1-*x*} thin films. Post-ORR, the Mn film exhibits two clear oxidation features, a peak at 0.79 V (peak B, **Supplementary Fig. S14**) and a broad feature centered at 0.95 V vs. RHE (peak C, **Supplementary Fig. S14**); peak A in **Supplementary Fig. S14** may be present for the Mn film but hidden by the magnitude and broadness of peaks B and C. Ag₃₀Mn₇₀ shows these same oxidation features, as well as reduction peaks at 0.5 V and 0.19 V vs. RHE (peaks E and F, **Supplementary Fig. S14**). Post-ORR, the Ag-rich thin film group displays similar profiles with reduction peaks at around 0.8 V, 0.48 V, and 0.2 V vs. RHE (peaks D, E, F, **Supplementary Fig.**

S14), and oxidation peaks at around 0.55 V, 0.71 V, and 0.92 V vs. RHE (peaks A, B, C, **Supplementary Fig. S14**). While the Mn thin film exhibits different oxidation peaks and shifted reduction peaks before and after ORR cycling, suggesting surface oxidation changes due to electrochemical cycling, the Ag-rich samples have qualitatively similar redox profiles (comparing to each other in this group) before and after ORR (**Supplementary Fig. S14**), indicating that, on average, any *in situ* surface structure changes are small. The distinct redox profiles of the Mn-rich and the Ag-rich samples indicate intrinsically different redox dynamics, which may help to explain the differences in ORR activity. Specifically, more redox features are seen for $x = 70, 90, 95 \%$ than for pure Mn and $x = 30 \%$, suggesting that various Mn oxidation states can be promoted at the working electrochemical conditions when Ag is present at a significant amount in the near-surface. For example, Mn mixing with enough Ag may facilitate/promote more higher valent oxides, namely Mn_2O_3 , Mn_3O_4 , and MnO_2 , which are known to be significantly more ORR active than MnO.^{13, 15, 17, 19, 22, 27-32} In addition, the larger oxidation current seen for pure Mn and $\text{Ag}_{30}\text{Mn}_{70}$ from 0.5 – 1 V vs. RHE and the lack of strong reduction features indicates that there are some oxide species formed in the anodic leg of the CV that are not significantly reduced in the cathodic leg of the CV. If MnO is indeed the dominant as-deposited surface species, as shown above based on the ORR, XPS and XAS results, it may be possible that it is the main surface species during reaction, until redox processes occur and generate other Mn-oxide species at the surface of the mixed Ag-Mn films as a function of time, Ag composition, and potential. The slight improvement seen for $\text{Ag}_{30}\text{Mn}_{70}$ relative to Mn may be due to a minor increase in other, more ORR active Mn-oxide species whose formation is facilitated by the interaction of Ag and Mn atoms or may simply be due to the presence of some Ag-only active sites at the surface. While difficult to pinpoint without *operando*, surface-sensitive spectroscopic techniques, the active Mn-oxide species present on our Ag-Mn electrocatalysts, and the way they electronically hybridize with Ag, likely play an important role in the observed ORR performance motifs. The composition–activity motifs vs. redox features trends for the $\text{Mn}_y\text{@Ag}$ thin films, shown in **Supplementary Fig. S26**, are similar to those seen for $\text{Ag}_x\text{Mn}_{1-x}$.

Supplementary Note S3: Extended SEM, EDS, AES discussion

While direct and clear compositional trends cannot be derived from SEM imaging alone, partly because of the large probe depth (on the order of microns) relative to the thin film thickness (70 nm) and Mn layer thickness on the $\text{Mn}_y\text{@Ag}$ films (i.e. 0.3–10 nm), **Supplementary Figs. S17–S19** generally support the hypothesis that the imaged thin films have a relatively homogenous composition and structure, as expected for polycrystalline thin films synthesized by *e*-beam PVD, and only exhibit minor topographical features (within technique resolution), generally more prevalent after ORR testing, and some of which could have different average compositions than the underlying film. While many factors such as adventitious carbon/organic contamination, surface and bulk composition, film thickness/height, conductivity, and sample charging, can complicate the interpretation of SEM images, we employed combined physical characterization with a plethora of other techniques, as discussing throughout this work, such as XPS, AES, AFM, EDS, and electrochemical cycling that help better understand the structure and composition our thin films before and after ORR testing.

As indicated by the backscattered electrons (BSE) imaging of the $\text{Ag}_{70}\text{Mn}_{30}$ thin film after reaction (**Supplementary Fig. S18a**), sample composition is likely highly homogeneous and has a few features visible in both the BSE and SE images (**Fig. S18a**). In the BSE images, these minor features appear as

aggregated grains and/or grains surrounded by darker grains, whereas in the secondary electrons (SE) images they appear darker than the surrounding film, indicating that they could have a different near-surface composition.

Looking at a representative as-deposited $\text{Mn}_{0.3\text{nm}}@\text{Ag}$ sample (**Fig. S18b,c**), in the BSE images, we see bright features that appear to be large grains that are either slightly taller or more enriched with Ag compared to the surrounding film, as well as some darker features that appear to be large grains or single crystallites. The darker features are apparent in both the BSE and SE images; since these do not appear on pure Ag films, it is possible these are MnO_x -rich regions.

The $\text{Mn}_{1\text{nm}}@\text{Ag}$ thin film post-ORR (**Fig. S18d**) appears to have a well-mixed composition, as indicated by the BSE imaging, with a few darker features visible in both the BSE and SE images (**Fig. S18d**). These darker features appear to have larger grains or be composed of a single crystallite, both of which could be consistent with a composition different than the surrounding film. Large grains are also observed throughout the film that are not contrasted in either BSE or SE images, indicating that these large grains that form are not necessarily consistent with a thicker film, or a change in the film composition. In the SE images, there are multiple bright nano-island-like features at the surface of the thin film that are not strongly contrasted in the BSE images (although this could be because for this particular image we didn't optimize the contrast); this indicates that these spots could have similar Ag content to the surrounding film, and are brighter in the SE images due to the sharp edge of these features and/or different surface compositions. While composition is difficult to discern based on SEM alone, AES mapping (**Supplementary Figs. S21,S22**) suggests these bright nano-island-like features seen the SE image (**Fig. S18d**) could be MnO_x -rich.

To have some qualitative comparison of the composition of the different samples with SEM imaging, we imaged these samples with BSE and SE in separate images, and at the same brightness and contrast in the same session (representative images shown in **Supplementary Fig. S19a–d**). Comparing the BSE images of Ag and MnO_x thin films (**Supplementary Fig S19a,b**), MnO_x is darker as expected because of its lower average atomic number compared to Ag; sample regions with lower atomic number will have less back scattering of electrons from atomic nuclei, and the number of detected BSEs correlates with image brightness. Comparing the $\text{Mn}_{1\text{nm}}@\text{Ag}$ thin films before and after ORR (**Supplementary Fig S19c,d**), there is a noticeable change in the brightness of the film in the BSE images. Before reaction, the $\text{Mn}_{1\text{nm}}@\text{Ag}$ thin film is noticeably darker than the Ag thin film (**Supplementary Fig. S19a,b**); since both films have about the same Ag layer thickness, this change in brightness is likely due the presence of the 1 nm Mn layer on top attenuating the BSE signal owing to its lower atomic number. Post-reaction, the $\text{Mn}_{1\text{nm}}@\text{Ag}$ film appears slightly darker, and based on XPS measurements (**Fig. 5a**) this is likely due to a slight decrease in film thickness owing the observed Mn dissolution during reaction and/or unavoidable adventitious contamination (e.g. carbon, with lower atomic number) during storage, transport, or imaging session. Observing SE images, the $\text{Mn}_{1\text{nm}}@\text{Ag}$ thin film appears to have developed noticeable nano-island-like bright circular features, 50 nm or smaller, throughout the surface (**Fig. S19c,d**); these bright spots could be from edges of features taller than the surrounding area, and are not clearly distinguishable on the BSE images. These raised features are also seen on SEM images taken in standard mode (**Fig. S17d**). These bright features on the SE images that are not brighter in the BSE images and, alternatively to or in addition to being raised features, could have a different surface composition than the surrounding thin film but the same total Ag content throughout the depth of the grain; this is consistent with these bright grains on the SE images being enriched with MnO_x as suggested by AES mapping (**Supplementary Fig. S21,S22**).

Looking at SEM-EDS (SEM in standard mode) of representative of $\text{Ag}_{90}\text{Mn}_{10}$ and $\text{Mn}_{1\text{nm}}@\text{Ag}$ post ORR testing in **Supplementary Fig. S7**, we see that in the co-deposited films Ag and Mn remain well-mixed on average, and that EDS is not sensitive enough to detect the ultra-thin layer of Mn on the sequentially synthesized films despite nano-island-like circular bright features being present on $\text{Mn}_{1\text{nm}}@\text{Ag}$ post-ORR SEM images. Probing elemental mixing with AES as shown by the representative SEM-AES maps in **Supplementary Fig. S6**, we see that for the most part (on most of the sample area) Ag and Mn are well mixed/dispersed in the near-surface of both the $\text{Ag}_x\text{Mn}_{1-x}$ and $\text{Mn}_y@\text{Ag}$ films before and after ORR testing. While most of the sample surface is observed to be smooth and featureless both before and after ORR (as shown by AFM and SEM, in **Supplementary Fig. S8** and **S17–S19**, respectively), both the $\text{Ag}_x\text{Mn}_{1-x}$ and $\text{Mn}_y@\text{Ag}$ films exhibit some nano-island-like domains particularly after ORR, that while contributing negligibly to surface area as indicated by AFM, may have a different composition than the surrounding area. Specifically, representative AES maps suggest that such features on $\text{Ag}_{70}\text{Mn}_{30}$ after ORR and after ORR stability testing (**Supplementary Fig. S16 and S15**) and $\text{Mn}_{1\text{nm}}@\text{Ag}$ post-ORR (**Supplementary Fig. S21–S22**) are likely MnO_x -rich while the surrounding area remains with well-mixed/dispersed Ag/ MnO_x . As seen in the SEM imaging before testing of $\text{Mn}_{0.3\text{nm}}@\text{Ag}$ (**Supplementary Fig. S17**), the as synthesized $\text{Mn}_y@\text{Ag}$ films with low Mn coverages can also exhibit nano-island-like topographical domains, and representative AES mapping of similar features in as-synthesized $\text{Mn}_{1\text{nm}}@\text{Ag}$ (**Supplementary Fig. S20**) suggest that before reaction the near-surface of these features has well-mixed Ag and Mn with a slightly higher Ag content than the surrounding area (within technique resolution). **Supplementary Figs. S21–S22** suggest that these scarce nano-island-like domains become MnO_x -rich after ORR. Outside of these nano-island-like domains AES mapping suggests that the Ag and MnO_x are well-mixed in the near-surface of all the $\text{Ag}_x\text{Mn}_{1-x}$ and $\text{Mn}_y@\text{Ag}$ films before and after ORR (**Supplementary Figs. S20–S22**). It is important to note that there are some convoluting factors that may prevent AES from being quantitative, namely buildup of adventitious carbon during measurement, image drift during measurement (best images are provided in this work), and the fact that intensity, not integrated area, is what is recorded during mapping. Moreover, it's noteworthy that the Mn signal highly overlaps with that of O, so the measured intensity is more representative of MnO_x assuming, as suggested by Su XPS (**Supplementary Fig. S2**) that most of the O signal arises from MnO_x and not from the adventitious carbonaceous contamination. Finally, it is important to note that the exact top-most atomic layer Ag/Mn composition of nano-island-like domains remains an open question, as the most surface sensitive techniques available to us probe at least several nanometers.

References

1. S. Tougaard and C. Jansson, *Surf. Interface Anal.*, 1993, **20**, 1013-1046.
2. M. C. Biesinger, B. P. Payne, A. P. Grosvenor, L. W. M. Lau, A. R. Gerson and R. S. C. Smart, *Appl. Surf. Sci.*, 2011, **257**, 2717-2730.
3. D. Higgins, M. Wette, B. M. Gibbons, S. Siahrostami, C. Hahn, M. Escudero-Escribano, M. García-Melchor, Z. Ulissi, R. C. Davis, A. Mehta, B. M. Clemens, J. K. Nørskov and T. F. Jaramillo, *ACS Appl. Energy Mater.*, 2018, **1**, 1990-1999.
4. D. Nečas and P. Klapetek, *Open Phys.*, 2012, **10**, 181-188.
5. M. Neville, *J. Phys.: Conf. Ser.*, 2013, **430**, 1-7.

6. Y. Gorlin, C. J. Chung, J. D. Benck, D. Nordlund, L. Seitz, T. C. Weng, D. Sokaras, B. M. Clemens and T. F. Jaramillo, *J. Am. Chem. Soc.*, 2014, **136**, 4920-4926.
7. J. A. Zamora Zeledón, G. A. Kamat, G. T. K. K. Gunasooriya, J. K. Nørskov, M. B. Stevens and T. F. Jaramillo, *ChemElectroChem*, 2021, **8**, 2467-2478.
8. J. A. Zamora Zeledón, M. B. Stevens, G. T. K. K. Gunasooriya, A. Gallo, A. T. Landers, M. E. Kreider, C. Hahn, J. K. Nørskov and T. F. Jaramillo, *Nat. Commun.*, 2021, **12 (620)**, 1-9.
9. R. Zhou, Y. Zheng, M. Jaroniec and S. Z. Qiao, *ACS Catal.*, 2016, **6**, 4720-4728.
10. C. V. Cushman, P. Brüner, J. Zakel, G. H. Major, B. M. Lunt, N. J. Smith, T. Grehl and M. R. Linfood, *Analytical Methods*, 2016, **8**, 3419-3439.
11. M. Rabe, C. Toparli, Y.-H. Chen, O. Kasian, K. J. J. Mayrhofer and A. Erbe, *Phys. Chem. Chem. Phys.*, 2019, **21**, 10457-10469.
12. B. M. Gibbons, M. Wette, M. B. Stevens, R. C. Davis, S. Siahrostami, M. Kreider, A. Mehta, D. C. Higgins, B. M. Clemens and T. F. Jaramillo, *Chem. Mater.*, 2020, **35**, 1819-1827.
13. S. Sun, H. Miao, Y. Xue, Q. Wang, S. Li and Z. Liu, *Electrochim. Acta*, 2016, **214**, 49-55.
14. S. A. Park, H. Lim and Y. T. Kim, *ACS Catal.*, 2015, **5**, 3995-4002.
15. I. Shypunov, N. Kongi, J. Kozlova, L. Matisen, P. Ritslaid, V. Sammelselg and K. Tammeveski, *Electrocatalysis*, 2015, **6**, 465-471.
16. H. Huang, Y. Meng, A. Labonte, A. Doble and S. L. Suib, *J. Phys. Chem. C*, 2013, **117**, 25352-25359.
17. D. A. Slanac, A. Lie, J. A. Paulson, K. J. Stevenson and K. P. Johnston, *J. Phys. Chem. C*, 2012, **116**, 11032-11039.
18. J. Liu, J. Liu, W. Song, F. Wang and Y. Song, *J. Mater. Chem. A*, 2014, **2**, 17477-17488.
19. Q. Wu, L. Jiang, L. Qi, L. Yuan, E. Wang and G. Sun, *Electrochim. Acta*, 2014, **123**, 167-175.
20. M. A. Kostowskyj, D. W. Kirk and S. J. Thorpe, *Int. J. Hydrog. Energy*, 2010, **35**, 5666-5672.
21. Q.-m. Wu, J.-m. Ruan, Z.-c. Zhou and S.-b. Sang, *Trans. Nonferrous Met. Soc. China*, 2015, **25**, 510-519.
22. F. W. T. Goh, Z. Liu, X. Ge, Y. Zong, G. Du and T. S. A. Hor, *Electrochim. Acta*, 2013, **114**, 598-604.
23. Y. Gorlin, B. Lassalle-Kaiser, J. D. Benck, S. Gul, S. M. Webb, V. K. Yachandra, J. Yano and T. F. Jaramillo, *J. Am. Chem. Soc.*, 2013, **135**, 8525-8534.
24. B. Hammer and J. K. Nørskov, Academic Press, 2000, vol. 45, pp. 71-129.
25. M. Łukaszewski, M. Soszko and A. Czerwiński, *Int. J. Electrochem. Sci*, 2016, **11**, 4442-4469.
26. Y. Yoon, B. Yan and Y. Surendranath, *J. Am. Chem. Soc.*, 2018, **140**, 2397-2400.
27. K. A. Stoerzinger, M. Risch, B. Han and Y. Shao-Horn, *ACS Catal.*, 2015, **5**, 6021-6031.
28. K. L. Pickrahn, S. W. Park, Y. Gorlin, H.-B.-R. Lee, T. F. Jaramillo and S. F. Bent, *Adv. Energy Mater.*, 2012, **2**, 1269-1277.
29. Y. Gorlin and T. F. Jaramillo, *J. Am. Chem. Soc.*, 2010, **132**, 13612-13614.
30. Y. Gorlin, C.-J. Chung, D. Nordlund, B. M. Clemens and T. F. Jaramillo, *ACS Catal.*, 2012, **2**, 2687-2694.
31. J. W. D. Ng, Y. Gorlin, D. Nordlund and T. F. Jaramillo, *J. Electrochem. Soc.*, 2014, **161**, D3105-D3112.
32. L. Mao, D. Zhang, T. Sotomura, K. Nakatsu, N. Koshiba and T. Ohsaka, *Electrochim. Acta*, 2003, **48**, 1015-1021.